Necroptosis inhibition counteracts axonal degeneration, cognitive decline and key hallmarks of aging, promoting brain rejuvenation.

Macarena S. Arrázola[1,2], Matías Lira[3], Gabriel Quiroz[2], Somya Iqbal[4], Samantha L Eaton[4], Rachel A Kline[4], Douglas J Lamont[4], Hernán Huerta[1,2], Gonzalo Ureta[5], Sebastián Bernales[5], J César Cárdenas[1,2,6,7], Waldo Cerpa[3,8], Thomas M. Wishart[4] and Felipe A. Court [1,2,6,*].

[1] Center for Integrative Biology, Faculty of Sciences, Universidad Mayor

[2] Geroscience Center for Brain Health and Metabolism (GERO), Santiago, Chile.

[3] Departamento de Biología Celular y Molecular, Facultad de Ciencias Biológicas, Pontificia Universidad Católica de Chile, Av. Libertador Bernardo O´Higgins 340, Santiago, Chile.

[4] The Roslin Institute, University of Edinburgh, Edinburgh, UK.

[5] Fundación Ciencia & Vida, Santiago, Chile.

[6] Buck Institute for Research on Aging, Novato, CA, USA.

[7] Department of Chemistry and Biochemistry, University of California, Santa Barbara, California, USA

[8] Centro de Excelencia en Biomedicina de Magallanes (CEBIMA), Universidad de Magallanes, Punta Arenas, Chile.

* Contact information: felipe.court@umayor.cl

Abstract

Age is the main risk factor for the development of neurodegenerative diseases. In the aged brain, axonal degeneration is an early pathological event, preceding neuronal dysfunction, and cognitive disabilities. Necroptosis activation mediates degeneration of injured axons, but whether necroptosis triggers neurodegeneration and cognitive impairment along aging is unknown. Here we show necroptosis activation in hippocampal axons during aging. Loss of the necroptotic effector *Mlkl* was sufficient to delay age-associated axonal degeneration, protecting against decreased synaptic transmission and memory decline in aged mice. Moreover, short-term pharmacologic inhibition of necroptosis in aged mice reverted structural and functional hippocampal impairment. Finally, a quantitative proteomic analysis revealed that necroptosis inhibition leads to an overall improvement of the aged hippocampal proteome, including molecular biofunctions associated with brain rejuvenation. Our results demonstrate that necroptosis contributes to the functional decline of the aged brain, and necroptosis inhibition constitute a potential geroprotective strategy to treat age-related disabilities.

1. INTRODUCTION

The current rise in human life expectancy is not precisely accompanied by an equivalent increase in 'healthspan'[1], the functional and disease-free period of life in the elderly[2]. The impact of age on brain function is unquestionable, being the main risk factor for the development of neurodegenerative diseases and cognitive disabilities[3–5].

As a fundamental structure for human cognition, the hippocampus is particularly vulnerable to the deleterious effects of aging[6,7]. Microstructural changes at the synaptic level are correlated with learning and memory impairment during aging. Decreased number of axospinous synapses have been described in the dentate gyrus of aged hippocampus[8]. The reduced number of synaptic contacts is correlated with a decreased presynaptic fiber potential due to a reduction of axons[9], contributing to the impaired synaptic plasticity and cognitive deficits evidenced in aged organisms[10]. In addition, white matter abnormalities and axonal degeneration (AxD) have been identified in aged brains of diverse species[11,12], particularly in the hippocampus and strictly correlated with impaired memory performance in humans[13]. Due to the importance of axonal integrity on hippocampal function and progression of cognitive decline in the elderly[14], it is imperative to determine the mechanism of AxD during aging. We were pioneers in identifying necroptosis as the mechanism involved in mechanical and chemical-induced AxD[15,16]. Recently, in a model of neuronal inflammation it has been demonstrated that necroptosis activates Sarm1, a central executioner of pathological AxD[17–19]. Necroptosis is an alternative form of programmed cell death triggered by the tumor necrosis factor under caspase-8 inhibitory conditions and characterized by a necrotic-like and pro-inflammatory response[20,21]. Receptor-interacting kinase 1 (RIPK1) recruits and phosphorylates RIPK3, which in turn phosphorylates the mixed lineage kinase domain-like protein (MLKL). MLKL oligomerizes and translocate to the plasma membrane, disrupting membrane integrity followed by the release of cellular components, an exacerbated inflammatory response, and cell death[22].

Age-associated increase in low-grade sterile inflammation is one of the 'seven pillars of aging' contributing with the development and progression of age-associated diseases[23–25]. Recent studies have depicted the importance of necroptosis in the aging of the mouse male reproductive system[26] and the epididymal white adipose tissue[27]. In the context of brain aging, several age-related neurodegenerative conditions with prominent AxD and neuroinflammation as common features have shown increased necroptosis activation in the brain, associated with functional impairment[28–32]. Necroptosis activation has been recently described in the cortex and hippocampus of aged mice, contributing to age-related neuroinflammation[33]. However, the involvement of necroptosis in the progression of normal brain aging and its cognitive consequences remain unexplored.

Here, we investigated the role of necroptosis in the progression of AxD in the hippocampus and its impact in brain function along aging. Necroptosis increased in hippocampal subfields with evident AxD in aged mice. Loss of *Mlkl* was sufficient to delay age-related AxD in the hippocampus, a youthful

phenotype also displayed at the synaptic and functional level. Restored synaptic transmission and facilitation were accompanied by improved learning and memory in aged mice deficient for *Mlkl*. Short-term inhibition of RIPK3 in aged mice demonstrated to be extraordinarily effective on reverting AxD and hippocampus-dependent functional impairment. Finally, an unbiased quantitative proteomic analysis demonstrated that necroptosis inhibition improved the aged hippocampal proteomic profile, restoring the levels of key protein pathways associated with brain aging hallmarks. Our study reveals that necroptosis contributes to the age-associated deterioration of axons and their function, affecting hippocampal neuronal connectivity and cognitive function of aged mice.

Taken together, our data demonstrates that necroptosis inhibition constitute a potential strategy for the future development of therapeutic tools to treat age-related brain disabilities and brain rejuvenation.

2. RESULTS

2.1. Brain aging is associated with axonal degeneration in the hippocampal dentate gyrus.

In order to establish the progression of hippocampal neurodegeneration throughout aging we used three groups of mice of different ages: adult (3-6 months), old (12-15 months) and aged (more than 20 months). Neurodegeneration, evaluated by Fluoro Jade C (FJC) staining (**Fig 1a**), significantly increases in the dentate gyrus (DG) of the hippocampus of old mice, reaching a plateau in the aged group (**Fig 1b**). Increased neurodegeneration was restricted to the DG hilus, where DG granular neurons extend their axons, known as mossy fibers, to connect with CA3 pyramidal neurons[34]. FJC staining was also analyzed in other brain regions, as the striatum, cerebellum and spinal cord, in which age-dependent neurodegeneration was also evident (**Fig S1**).

To further evaluate age-associated AxD in the hippocampus, we studied the expression of two phosphorylated forms of neurofilaments (NFs), the main proteins shaping the axonal cytoskeleton. Most NFs are highly phosphorylated under physiological conditions, while increased non-phosphorylated NF (non-pNF) immunoreactivity is associated with inflammation, neurodegenerative diseases and brain injury[35,36]. Almost undetectable immunoreactivity of non-pNF was observed in the DG of adult mice, while a progressive increase was evidenced during aging (**Fig 1c, d**). Axonal degeneration evaluated by pan-axonal-NF detection (stable axonal NFs) (**Fig 1e**) showed decreased axonal integrity index in old and aged hippocampal DG compared with adult mice (**Fig 1f**). Therefore, by using different degenerative readouts, our results illustrate the progression of AxD in the hippocampus during aging.

2.2. Necroptosis activation in hilar cells and axonal fibers in the dentate gyrus of the aged hippocampus.

Previous studies have indicated that axons degenerate by an apoptosis-independent mechanism[37,38]. We recently demonstrated that mechanical and chemical-induced axonal degeneration is regulated by necroptosis[15]. To determine whether necroptosis is involved in age-associated AxD, we assessed necroptosis activation by the expression of the phosphorylated form of MLKL (pMLKL) in the hippocampus. The analysis was performed in the hilus and the granular cell layer (GCL) of the DG (**Fig 2b**). The number of pMLKL positive hilar cells increased in aged mice, as did pMLKL mean intensity (**Fig 2a, c**). Necroptosis activation was also evidenced by an age-dependent translocation of pMLKL from the nucleus to the cytoplasm (**Fig 2a**, magnified image), as has been previously described[39]. Non-significant changes in pMLKL levels were observed in GCL neurons (data not shown), suggesting a selective vulnerability of DG hilus to necroptosis activation during aging. Axonal pMLKL staining was evaluated in pan-axonal-NF positive hilar fibers of the DG (**Fig 2d**). Interestingly, pMLKL mean intensity increased earlier in DG axons compared with dentate hilar somas throughout aging, reaching significant differences in the old mice group (**Fig 2e**). Increased pMLKL signal was also observed in other brain regions with defined axonal subfields, as axonal tracts in the striatum, the cerebellar white matter and the ventral horn of the spinal cord, which also showed progressive AxD along aging (**Fig S2**). The increase in MLKL phosphorylation levels in the hilus was also accompanied by changes in the pattern of pMLKL signal, from almost non-detected in adult mice axons, diffuse in the old group, to finally become punctuated in fragmented axons of aged mice (**Fig 2d**, magnified image). These pMLKL aggregates have been associated with MLKL oligomerization and its translocation to the plasma membrane, two key steps for necroptosis execution[22]. A similar pattern of pMLKL was observed by immunohistochemistry against pMLKL in the aged hippocampus, both in DG hilar cells and in Schaffer collateral axons (**Fig 2f**), which connect with CA1 pyramidal neurons. These results indicate that necroptosis is activated during aging in the hippocampus, particularly in the DG hilus, an hippocampal region recognized as one of the most vulnerable to the cognitive effects of aging[40].

2.3. Age-induced axonal degeneration is reduced in MLKL knockout mice.

Due to the indispensable role of MLKL in executing necroptosis, we evaluated whether age-dependent AxD in the hippocampus was modified in aged *Mlkl*-knockout mice (*Mlkl*-KO)[41]. Interestingly, AxD evaluated with a degeneration index (DI) in pan-axonal NF-stained axons was significantly reduced in aged *Mlkl*-KO mice at levels comparable with adult mice (**Fig 3a, b**). Moreover, non-pNF degenerated axons profusely present in aged WT hippocampus, were almost undetected in aged *Mlkl*-KO mice, at levels equivalent to younger WT mice (**Fig 3a, c**). As expected, we observed age-dependent AxD coupled with neuroinflammation[42] (**Fig S3**). The increased number of microglia in the hippocampus of aged mice was prevented in aged *Mlkl*-KO mice (**Fig S4**), as was previously described[33]. Accordingly, measurement of Iba1 mean intensity also indicated that aged *Mlkl*-KO mice present less microglia activation than their WT littermates (**Fig 3d, e**). To confirm the contribution of necroptosis to the inflammatory state of the aging brain, we measured the levels of

several cytokines and chemokines in hippocampal lysates and serum of adult versus aged WT and *Mlkl*-KO mice by Luminex High Performance Assay (**Table S1**). Three of the twelve cytokines analyzed showed significant changes under *Mlkl* deficiency in the hippocampus of aged mice. The levels of the pro-inflammatory cytokine IL-12 decreased in aged *Mlkl*-KO hippocampus compared with aged WT mice, reaching levels comparable with adult WT mice (**Fig 3f**). Interestingly, the anti-inflammatory cytokines IL-2 and IL-10 significantly increased in the hippocampus of aged *Mlkl*-KO mice (**Fig 3f**). Moreover, the systemic pro-inflammatory profile also decreased in serum samples from aged *Mlkl*-KO mice (**Fig S5**). These results indicate that necroptosis contributes to brain inflammation by modulating both pro- and anti-inflammatory cytokines, but also controlling systemic inflammation.

2.4. Loss of MLKL improves hippocampal synaptic transmission, learning and memory in aged mice.

To further study whether necroptosis-mediated AxD affects hippocampal function along aging, we first performed electrophysiological recordings of the CA3-CA1 synapses to evaluate synaptic transmission. Extracellular field-excitatory post-synaptic potentials (fEPSP) were registered in hippocampal slices (**Fig 4a**). Average traces of the evoked potential recorded are represented in **Fig 4b** for each group. An age-dependent decrease in fEPSP slope was observed in WT mice. Nevertheless, in aged *Mlkl*-KO mice, the fEPSP slope was maintained at levels comparable to adult WT mice (**Fig 4c, d**). To specifically evaluate whether axonal alterations contribute to an age-dependent decrease in synaptic transmission, we analyzed the facilitation index ($fEPSP_2/fEPSP_1$) using a paired-pulse stimulation protocol (**Fig 4e**). The increased facilitation index observed in WT aged mice (**Fig 4f**) indicates a decreased neurotransmitter release probability from the axonal compartment (pre-synapse). Interestingly, the facilitation index of aged *Mlkl*-KO mice was comparable to adult WT mice (**Fig 4e, f**). These results indicate that *Mlkl* deficiency delays the loss of synaptic strength in the hippocampus inherent to brain aging, mainly preventing axonal function defects in aged mice.

Since memory capabilities depend on proper hippocampal function and both are affected by age[43,44], we evaluated whether *Mlkl* loss improves spatial learning and memory in aged mice. To this end, a Morris water maze (MWM) navigation task was performed in adult and aged *Mlkl* -KO mice and compared with their WT littermates. The learning curve of aged *Mlkl*-KO mice was significantly faster than those of aged WT animals and reached a reduced latency to find the platform from day 3 until the end of the training, showing comparable escape time to adult animals (**Fig 4g**). No differences were observed between adult WT and *Mlkl*-KO mice in the learning curve. To evaluate memory, 24 hours after training, mice were challenged to find the original location of the platform, which was removed. The differences between adult and aged *Mlkl* -KO and WT animals in the time spent in the quadrant platform (Q4) are shown in the swimming heatmap tracks shown in **Fig 4h**. Aged *Mlkl* -KO mice travelled a larger distance and spent more time exploring in the target quadrant

Q4 compared to aged WT animals (**Fig 4i, j**), without significant changes in the mean swimming speed between both groups (data not shown), demonstrating that loss of *Mlkl* prevents learning and memory loss associated with aging.

Altogether, these results demonstrate that an age-associated increase in brain necroptosis induces degeneration of axons in the dentate gyrus of the hippocampus, thereby depressing synaptic transmission, and impairing hippocampal-dependent functions, such as learning and memory in aged mice.

2.5. Pharmacological inhibition of necroptosis reverts key signs of brain aging, improving hippocampal function and memory.

To further explore the role of necroptosis in brain aging, we developed a pharmacologic strategy by using the selective RIPK3 inhibitor, GSK'872[45,46]. In order to evaluate whether necroptosis inhibition reverts age-associated alterations, we designed a strategy in which GSK'872 was systemically administrated in 23-month-old mice for only one month. Diffusion pumps were filled with vehicle or GSK'872, and intraperitoneally implanted to continuously diffuse the inhibitor (2 mg/kg GSK'872 at 0.11 µl/hr) for 28 days. In order to evaluate whether GSK'872 systemically administrated is capable to cross the blood brain barrier, we performed pharmacokinetic studies. Measurable levels of GSK'872 were detected 1h post administration in the brain (187.6 ± 17.11 nm) and plasma (18.32 ± 0.85 µm) samples collected from aged animals treated with a single i.p. dose of 10mg/kg of GSK'872. The efficiency of GSK'872 treatment in the brain was evaluated by measuring phosphorylated RIPK3 (pRIPK3) levels in the hippocampus, demonstrating decreased pRIPK3 signal in the hilus of aged GSK'872-treated mice (**Fig S6**). Remarkably, aged mice treated with GSK'872 showed decreased non-pNF staining in comparison to vehicle treated mice of the same age (**Fig 5a**). In fact, non-pNF levels in GSK'872 treated aged mice were comparable with those observed in adult animals (**Fig 5b and 3c**), demonstrating that one month of systemic RIPK3 inhibition reverts signs of AxD associated with brain aging. Moreover, decreased microglia activation was also observed, indicating that a short-term treatment with GSK'872 is capable of reverting one of the main signs of brain inflammation associated with aging (**Fig 5c, d**).

Since RIPK3 is involved in several pathways that regulate cytokines secretion and the inflammatory response[47] we performed Luminex High Performance Assay to detect changes in a pool of selected cytokines (**Tables S1**). Interestingly, the hippocampus of GSK'872 treated mice showed a pattern of cytokine levels highly similar to those observed in untreated adult mice (**Fig 5e**). Remarkably, this analysis reveals that RIPK3 inhibition mainly reduces pro-inflammatory cytokines, such as TNF-α, IL-6, IL-12, and IFN-γ, reaching youthful-like cytokine levels equivalent to adult mice (**Fig 5f**). A similar profile of decrease in pro-inflammatory cytokines was observed systemically in serum samples of GSK'872 treated mice, as was also noticed in the genetic model (**Fig S5**).

At the functional level, electrophysiological recordings in the hippocampus demonstrated equivalent fEPSP between aged mice treated with GSK'872 and untreated adult mice (**Fig 6a**). Average traces showed significant differences between aged vehicle-treated mice versus those that received the RIPK3 inhibitor (**Fig 6b,c**). To evaluate the axonal contribution on this protective effect of GSK'872 on synaptic transmission, we performed a paired-pulse stimulation protocol (**Fig 6d)**. Facilitation index was significantly lower in the hippocampus of aged mice treated with GSK'872 compared with the aged-vehicle mice (**Fig 6e**), showing that late and short-term necroptosis inhibition can revert the loss of synaptic strength in aged mice, by promoting axonal function.

To further explore the impact of our pharmacologic intervention on hippocampal-dependent behavioral skills we evaluated spatial learning and memory in aged GSK'872-treated mice. Remarkably, RIPK3 inhibition significantly improved learning in aged mice from the second day of training (**Fig 6f**). Memory assessment indicated that aged mice with GSK'872 treatment spent more time in the target quadrant and travelled larger distance in Q4 compared with aged vehicle-treated mice. Thus, RIPK3 inhibition is capable to recover aged mice from learning and memory impairment.

These results demonstrate that a short-term administration of GSK'872 can revert key hallmarks of brain aging, including AxD, neuroinflammation, and age-associated memory impairment, proposing the inhibition of necroptosis as an attractive therapeutic target to improve memory in the elderly.

2.6. Proteomic analysis in the hippocampus of aged mice with genetic and pharmacological inhibition of necroptosis reveals improvement in key hallmarks of aging and features of brain rejuvenation.

In order to elucidate the specific molecular alterations underpinning our necroptosis-inhibitory approaches toward reducing aging phenotypes, we employed a state-of-the-art single-shot, label free quantitative proteomic approach. Our aim was to generate a correlative necroptotic proteomic profile in order to gain insight toward how necroptosis or, conversely, its inhibition influences neuronal integrity in aging-associated degeneration. To this end, hippocampus of adult and aged WT mice, aged *Mlkl*-KO mice, and aged GSK'872-treated mice were subjected to single-shot label-free mass spectrometry (see workflow in **Fig S8a**), obtaining a high degree of coverage of the proteome with almost 7,000 proteins detected (**Fig S8b**).

To determine which molecular processes were likely correlative with the aging-induced necroptotic events, relative expression ratios were calculated and used to perform expression profile clustering analyses. We identified and isolated subsets of proteins exhibiting opposing directionality in expression between the "normal" aging proteome (aged vs adult animals) and the proteomes of animals subjected to genetic (aged *Mlkl*-KO vs aged WT) or pharmacological (aged GSK'872 vs aged vehicle) inhibition of necroptosis (**Fig S8 and Fig S9**). In doing so, it was possible to reduce the number of correlative candidate proteins to 2,516 proteins whose expression increases and 2,307

which decrease in the aging hippocampus and where genetic and pharmacological modulation leads to a degree of reversion (**Fig 7a**). Contextualization of these necroptosis-correlative clusters through pathway analysis confirmed opposing directionality in the activation status of numerous biological processes between "normal" and necroptosis-targeted aged animals. These include several canonical pathways and biological function annotations previously implicated in normal aging[23,25] (see hallmarks of aging, **Fig S10a**) and in brain rejuvenation[5,48] (**Fig 7b and Fig S10b**). Most of the molecular cascades belonging to these groups of pathways are typically associated with neurodegeneration and/or neuronal aging, including all the molecular cascades involved in *synaptic mechanisms, senescence* and *cellular homeostasis*, which are indeed affected in the normal aging proteome and recovered in the genetic and pharmacological models of necroptosis inhibition (**Fig 7b**).

In order to explore the contribution of necroptosis in age-associated neuronal dysfunction, we evaluated several biological functions affected by normal aging in our proteomic analysis. These biofunctions were classified considering their contribution in central brain functions, designated as *neurodegeneration, synaptic function, cognitive and behavior,* and *neuronal development*. It is interesting to note that the patterns of change of these biofunctions show opposing directionality in both the genetic and pharmacological approaches of necroptosis inhibition compared with normal aging in most of the biological functions analyzed (**Fig 7c**). Remarkably, key molecular and cellular functions associated with neurodegeneration, neuronal integrity and function, including cell survival and viability, cellular homeostasis, synapse development, cognition, motor dysfunction and cytoskeleton organization, showed a clear reversion in the context of pathway analysis in necroptosis-targeted aging in comparison with normal aging (**Fig 7c**). This analysis demonstrated that the inhibition of necroptosis supports proper brain function in aged animals, improving key hallmarks of aging and restoring (in the case of our pharmacologic treatment with GSK'872) relevant functions involved in brain rejuvenation.

2.7. Necroptosis inhibition induces synaptic-long term potentiation in aged mice.

Among the cascades elucidated in our proteomic analysis with clear opposed profiles between normal aging and necroptosis inhibitory conditions, those classified as *synaptic mechanisms* showed the highest predicted z-score. Synaptic long-term potentiation (LTP) is the most common studied form of synaptic plasticity, a key process directly related with learning and memory, and early impaired during aging[49]. The contribution of the synaptic LTP signaling at the level of individual molecules is visually illustrated in **Fig 8a.** These molecular changes are mostly prevented in the aging process of the *Mlkl*-KO mice (red molecules) and partially reverted in the pharmacologic inhibition of necroptosis with GSK'872 in aged animals (**Fig 8b**). We therefore analyzed hippocampal synaptic plasticity by studying LTP magnitude in the CA3-CA1 transmission. By the usage of a high-frequency stimulation protocol, we found that LTP induction was compromised in aged WT mice when compared to adult

WT mice (**Fig 8c**). Surprisingly, adult *Mlkl*-KO mice presented a higher LTP magnitude than the control WT group and the loss of *Mlkl* in aged mice restored LTP induction and maintenance beyond adult WT mice potentiation. Synaptic plasticity was also assessed in the pharmacological model of necroptosis inhibition in aged mice. Similar to KO experiments, we detected a reduction in LTP magnitude when we compared adult WT mice with aged vehicle-treated mice. Surprisingly, only one month of GSK'872 treatment was capable to improve LTP magnitude, reaching adult-like levels (**Fig 8d**), demonstrating that inhibition of necroptosis either by genetic knock-out of *Mlkl* or by pharmacologic RIPK3 inhibition improved or restore synaptic plasticity in aged mice, a synaptic process that is crucial to support brain rejuvenation[5].

2.9 Necroptosis activation contributes to the acquisition of the age-associated senescent phenotype in the hippocampus during aging.

The accumulation of senescent cells in aged tissue, including the brain, is one of the most common feature of aging[50,51]. As neuronal senescence has also been detected in the hippocampus of aged mice[52], we aimed to determine whether necroptosis contributes to the establishment of the senescent phenotype of hippocampal neurons along aging. From our proteomic data, the molecular changes associated to senescence are mostly prevented in the aging process of the *Mlkl*-KO mice and partially reverted in the pharmacologic inhibition of necroptosis with GSK'872 treatment in aged animals (**Fig S11**). Interestingly, the expression profile of two key proteins involved in the acquisition of the senescent phenotype, namely CDKN1B and NFκB1[53], is mainly reverted in both *Mlkl*-KO and GK'872-treated mice during aging (blue dotted insets, **Fig S11a** and **Fig S11b**). We therefore evaluated cell senescence by SA-βgalactosidase (SA-βgal) activity in the hippocampus of aged WT and aged *Mlkl*-KO mice. The accumulation of SA-βgal positive neurons was mainly observed in the CA2/3 subfield of the hippocampus of aged mice[52] (**Fig S11c**), but it was significantly lower in aged *Mlkl*-KO mice (**Fig S11c, d**). A reduced SA-βgal activity was also observed in the hippocampus of aged mice treated with GSK'872 compared with vehicle-treated animals (**Fig S11e, f**), reinforcing the data obtained from the proteomic analysis, which overall indicates that age-related activation of necroptosis contributes to the development of key pathological changes that are involved in brain aging.

Together our findings support the conclusion that necroptosis activation participates in the development of the major causes of brain disfunction during aging, including AxD, neuroinflammation, synaptic dysfunction and cognitive disabilities. By contrast, the inhibition of necroptosis prevents these major features of brain aging, restoring synaptic transmission and axonal function in the hippocampal circuitry, thus improving learning and memory defects associated with aging. Furthermore, a short systemic inhibition of necroptosis was capable to revert age-associated hippocampal changes and restore learning and memory capacity to youthful levels.

3. DISCUSSION

Our findings reveal the involvement of necroptosis in the progression of AxD in the hippocampus during normal aging, uncovering relevant implications of necroptosis activation in age-associated cognitive impairment, which might undermine healthy aging. Of note, most detrimental consequences of brain aging, including neuroinflammation, synaptic failure and hippocampal-dependent behavioral impairment were prevented through inhibition of necroptosis by genetic or pharmacological means. In our mouse model of aging, neurodegeneration appears to be restricted to axonal-enriched brain regions, such as the corpus striatum, the cerebellum, and white matter regions of the spinal cord (**Fig 1** and **S1**). Corresponding with this observation, neurodegeneration was also noted in hippocampal subfields recognized as the richest axonal projection regions, including DG-CA3-CA1 axonal pathways[54]. Importantly, necroptosis activation was also confined to these axonal-enriched areas of the hippocampus, particularly in the DG (**Fig 1**), which is the only subfield that has been shown to present neuronal loss as a consequence of aging in humans[55]. The DG is a crucial area in the hippocampus supporting neuronal connectivity. It receives entorhinal cortex information which is transmitted to the CA3-CA1 neurons to complete the hippocampal circuitry. DG neurons, particularly mossy cells of the hilus, are extremely vulnerable to degenerative insults and injury, whereas DG granule cells are more resistant[56,57]. This evidence is aligned with our results showing increased necroptosis in hilar cells, and an early activation in the hilar fibers of the DG along with aging (**Fig 2**). Moreover, it has been shown that this confined subdivision of the hippocampus where mossy cells reside is also highly vulnerable to the effects of aging[55], compromising DG connectivity with other subfields of the hippocampus, and increasing susceptibility to memory failure in aged individuals[58,59]. These observations suggest that the restricted activation of necroptosis in DG hilar cells and axons may contribute to the vulnerability of this area to degenerate along with aging, to adversely impact synaptic function and hippocampal-dependent behavioral performance.

The functional role of necroptosis as a crucial pathogenic determinant in experimental models of human diseases has been of increasing interest in the field, focusing on the central effectors of necroptosis, RIPK3 and MLKL, as possible markers of disease progression and severity in humans[60]. Increased pMLKL levels in aged mice suggests that necroptosis could be considered as a biomarker of aging progression. Of note, aged *Mlkl*-KO mice presented a youthful phenotype in the hippocampus, reaching levels of AxD comparable with those observed in younger mice (**Fig 3a, b**). According to the survival curve comparison between mice and humans[61], old mice (12-15 months old) are equivalent to humans between 38 to 47 years old, a life stage in which basal levels of pMLKL were only slightly detected in the hippocampus (**Fig 2**). Interestingly, there is no incidence of dementia and cognitive impairment at this stage of life in humans going through a normal aging process (without inherited conditions and/or associated pathologies)[62], suggesting that maintaining necroptosis at lower activation levels could prevent age-associated pathological conditions.

As a chronic inflammatory condition, aging also influences the inflammatory status of the brain[23], mainly through microglia activation and increase of pro-inflammatory cytokines[63]. Among the pro-inflammatory cytokines analyzed in the hippocampus of aged *Mlkl*-KO mice only IL-12 decreased, reaching levels comparable with adult mice (Fig 3f). IL-12 is produced in the brain by microglia and required for IFN-γ and TNF-α production, two master inflammatory cytokines. The increased expression of IL-12 in the brain has been associated with spontaneous neurological disorders in aged mice[64]. By contrast, the IL12-KO mouse exhibits lower levels of microglia activation and reduced neurodegeneration in an excitotoxicity-mediated injury model[65]. Additionally, increased levels of the anti-inflammatory cytokines, IL-2 and IL-10, were specifically detected in aged *Mlkl*-KO mice (**Fig 3f**), suggesting that MLKL could also act as a repressor of anti-inflammatory cytokine expression under necroptosis activated conditions. Interestingly, IL-10 inhibits the production of IL-12[66], which accompanied with the IL-12 decrease observed in the aged *Mlkl*-KO mice generates a positive anti-inflammatory feedback loop in conditions of *Mlkl* deficiency, limiting neuroinflammation.

It is well documented that neurodegeneration contributes to cognitive decline during normal aging [67]. Hippocampal-dependent functions are determined by accurate electrophysiological signals. Loss of *Mlkl* in aged mice produces changes in the hippocampal circuit that prevent the loss of synaptic strength observed in normal aging (**Fig 4d**). The increased facilitation index observed in aged WT mice (**Fig 4f**) is an indicator of a decreased neurotransmitter release probability from the presynaptic compartment, which suggests hippocampal axonal failure in aged mice. Remarkably, the decreased paired-pulse facilitation index in aged *Mlkl*-KO mice indicates that necroptosis is in fact contributing to these axonal defects in aged mice. Electrophysiological results were supported by improved learning and memory performance in aged *Mlkl*-KO mice, demonstrating that altogether axonal protection, controlled inflammatory status, as well as synaptic transmission restoration in *Mlkl* deficiency favor youthful-like behavior in aged mice. These observations support the notion that lower levels of necroptosis activation improves key cognitive functions that might positively impact the quality of life, favoring healthy aging.

Multiple efforts have been made in the field of geroscience to understand the aging process and to consider it as a therapeutical target to improve healthspan[2,23,68]. The brain and peripheral organs share common biological mechanisms of aging[25]. Thus, the development of anti-aging drugs that improve cognitive function and hence the quality of life in old age could have a significant potential at improving healthspan. Our pharmacological strategy to systemically inhibit RIPK3 with GSK´872 in aged mice demonstrated to be extraordinarily effective on reverting AxD, neuroinflammation and hippocampus-dependent functional impairment (**Fig 5** and **Fig 6**). Interestingly, GSK'872 treatment reduced the levels of most of the pro-inflammatory cytokines analyzed in the hippocampus of aged mice, indicating that systemic inhibition of necroptosis impacts the inflammatory status of the brain, thereby diminishing neuroinflammation. Moreover, the analysis of serum cytokines showed the same

394 regulatory profile as the brain, demonstrating that systemically, the inflammatory condition of aged
395 mice is maintained in a youthful-like state under necroptotic inhibitory terms.

396 Our quantitative proteomic analysis allowed us to generate a correlative necroptotic proteomic
397 profile and to evaluate whether necroptosis inhibition influences key networks involved in brain aging.
398 The analysis demonstrated that about 7,000 proteins changed their expression profile as a
399 consequence of aging (**Fig 7** and **Fig S9**), of which 2,516 shown to be upregulated and 2,307 were
400 downregulated under necroptosis inhibitory conditions in the hippocampus of aged mice (**Fig S9**).
401 From these clustered profiles we were capable to contextualize these proteomic changes by
402 associated them with related canonical pathways and biological function annotations. The pathways
403 analysis unveiled key biological processes with opposed directionality between “normal” and
404 necroptosis-targeted aging, showing that key hallmarks of aging, including synaptic function,
405 mitochondrial dysfunction, stress response, cellular senescence, deficient nutrient sensing, altered
406 metabolism, and others[23,25], are positively regulated under necroptosis inhibitory conditions (**Fig S8**),
407 which may have potential impact in life quality by promoting healthy aging. Interestingly, our
408 pharmacological approach demonstrated a similar trend in effect over the proteome as the genetic
409 model, suggesting that necroptosis inhibition could be an attractive therapeutic strategy to develop
410 geroprotector agents to slow aging. In fact, results obtained from our proteomic analysis indicated
411 that GSK’872 treatment influences most of the different hallmarks of aging, an inclusion criteria that
412 is currently recognized to accept novel molecule candidates as geroprotectors[69]. Furthermore,
413 inhibition of necroptosis demonstrated ability to modulate several brain functions implicated in brain
414 rejuvenation[5] (**Fig 7** and **Fig S10**), including those elucidated from the proteomic analysis and
415 experimentally evaluated, such as synaptic plasticity and neuronal senescence (**Fig 8** and **Fig S11**),
416 which added to the behavioral results on learning and memory, reinforced the potential of GSK’872
417 as a candidate drug to protect against age-associated brain dysfunction, including memory decline.
418 Moreover, other interesting pathways were also demonstrated to be positively modulated by
419 necroptosis inhibition (see **Fig S12-S15** for individual molecular changes and proteomic profiles).
420 These pathways include *synaptogenesis signaling*, *calcium signaling*, *CREB signaling in neurons,*
421 and others; most of them highly implicated in the maintenance of neuronal homeostasis and
422 functioning, and consequently in brain-dependent functions, including cognitive and behavioral
423 processes[70].

424 Overall, our study demonstrates that necroptosis contributes to the age-associated deterioration of
425 axonal integrity and function, affecting hippocampal neuronal connectivity, and consequently the
426 cognitive function of aged mice. Our results from the pharmacological intervention propose
427 necroptosis inhibition as an interesting and novel therapeutic target to counteract the deleterious
428 effects of aging, thus increasing healthspan and potentially delaying the onset of a range of age-
429 related disabilities.

4. METHODS

4.1. Animals

Wild-type (WT) C57BL/6J mice of different ages were purchase from the Jackson Laboratory and maintained in the Universidad Mayor animal facility. Aging groups were established as follow: adult (3-6 month), old (12-15 month) and aged mice (more than 20 month). *Mlkl* knockout mice (*Mlkl*-KO) were kindly provided by Dr Douglas Green (St. Jude Children's Research Hospital, Memphis, TN, USA) and have been previously produced and described[71]. The age range was selected in equivalence with the human life phases[61,72]. Animals were kept under standard conditions of light and temperature and were feed with food and water ad libitum in the Animal Facility of the Sciences Faculty of the Mayor University. The research protocol no. 22–2017 was approved by the Animal Care and Use Scientific Ethic Committee of the Mayor University.

4.2. Osmotic pump implantation

Micro-osmotic pumps (Alzet, model 1004) containing the RIPK3 inhibitor GSK'872 (Tocris) (2 mg/kg) were surgically implanted in the peritoneal cavity of 23-moth-old. The pump allows a constant flux of the drug at 0.11 µl/hr for 28 days. One-month post-surgery, mice (24-month-old) were subjected to behavioral test to evaluate memory and then tissue was extracted for further analyses.

4.3. Quantification of GSK'872 in brain and plasma

Brain and plasma samples were obtained from aged mice treated for 1h with GSK'872 (10mg/kg i.p.). The bioanalysis of plasma and brain samples was conducted by LC-MS/MS with a QTRAP 4500 triple quadrupole mass spectrometer (Applied Biosystems SCIEX) in the negative ion mode and interfaced with an Ekspert ultraLC 100-XL UHPLC System (Eksigent). Calibration standards (0.003 to 10 µM) and quality controls (0.02, 0.2 and 2.0 µM) were prepared from naïve mouse plasma in parallel with mouse plasma study samples (60 µL) by precipitation with three volumes of ice-cold acetonitrile containing 20 µM of theophylline. The precipitated samples were centrifuged at 6,100 g for 30 min at 4°C. Following centrifugation, an aliquot of each supernatant was transferred to an autosampler vial and diluted with two volumes of aqueous mobile phase (0.2% formic acid in water). Samples were injected onto a reverse phase analytical column (YMC Triart C18; 2.0 x 50 mm; 1.9 µm; YMC CO) and eluted with a gradient of 0.2% formic acid in Acetonitrile. GSK'872 was monitored by a multiple reaction monitoring (MRM) experiment using an Analyst software (v1.6.2, Applied Biosystems SCIEX). Quantitation was conducted using a MultiQuant software (v2.1, Applied Biosystems SCIEX) and the resulting calibration curve was fitted with a linear regression and 1/x weighting. The lower limit of quantitation (LLOQ) was 0.010 µM.

4.4. Immunohistochemistry

Mice were deeply anesthetized with isoflurane and intracardially perfused with isotonic saline followed by 4% paraformaldehyde. Brains were dissected, postfixed overnight in 4% paraformaldehyde at 4 °C, and then incubated in 30% sucrose. Tissue was cryoprotected in optimal cutting temperature compound (OCT, Tissue-Tek) at −20 °C and serial sagittal sections of 20 µm thickness were obtained using a cryostat (Leica, CM1860). Brain sections were pre-mounted on positively charged slides and washed in TBS. After antigen retrieval (80 ˚C, 30 min, 10 mM citrate buffer, pH 6.0), sections were blocked in TBSB (TBS, 5% BSA and 0.25% Triton X-100), and then incubated overnight at 4 °C with the following primary antibodies: pMLKL (1:200, phospho S345, Abcam, ab196436), neurofilament pan-axonal cocktail (1:250, SMI312 clone, Biolegend), non-phosphorylated neurofilament (1:250, SMI32 clone, Biolegend), and Iba1 (1:500, Wako Chemicals, 016-26721). Sections were washed to remove the excess of primary antibody and incubated with the appropriate Alexa-Fluor secondary antibodies for 2 h at 25 °C (1:1000, Thermo Fisher Scientific). The excess of secondary antibody was washed, and the sections were coverslipped with Fluoromount-G antifade mounting medium (EMS, 17984-25) containing DAPI staining for nuclei detection (Thermo Fisher Scientific). For Fluoro-Jade C staining, brain tissue was mounted on positively charged slides and rehydrated on decreasing concentrations of ethanol. After rehydration, the tissue was pre- treated for 10 min in potassium permanganate and then incubated for 10 min in the dark at 25 °C in Fluoro-Jade C and DAPI (Biosensis, TR-100-FJ). The tissue was then washed with water and let dry overnight. The next day the slides were cleared in xylene and coverslipped with DPX-new mounting solution (Merck Millipore). The anti-pMLKL antibody purchase from Abcam (ab196436) was KO-validated by comparison of the immunodetected signal in aged WT mice with the *Mlkl*-KO mice in the hippocampus (**Fig S7**). Immunostained sections were scanned in a Leica DMi8 Fluorescence Microscope fully automatized.

4.5. Histological Analysis

Free-floating sections were processed for immunohistochemistry as previously described[31]. Briefly, slices were quenched with 0.3% H_2O_2 for 30 min, blocked with 5% BSA and 0.2% triton X-100 for 2 h and incubated with primary antibody (rabbit anti-pMLKL, 1:200 Abcam) overnight at 4 °C. Then, sections were washed with 0.1 M PBS and incubated with secondary biotinylated antibody (goat anti-rabbit, 1:500 Vector Laboratories) for 2 h at RT. After washing, slices were incubated with avidin–biotin–peroxidase complex (Vector Laboratories) for 1 h at RT followed by 0.1 M PBS washes and developed with 3,3-diaminobenzidine (DAB, Sigma-Aldrich). Finally, sections were co-stained with Nissl (cresyl-violet staining) to detect nuclei and with Eriochrome-C staining for myelinated-axons detection, and finally mounted on glass slides with Entellan medium (Merck).

4.6. Image Analysis

Fluorescent images were analyzed using the Image J software from the NIH, USA. Axonal degeneration index (DI) was measured in pan-axonal immunostained images as the ratio of the area of fragmented axons against the total axonal area (intact + fragmented particles) in the hilus using

the particle analyzer algorithm of ImageJ. Fragmented and intact axonal particles were estimated by defining area and circularity of the particles (fragmented: <20 μm^2 and 0.3 ≤ 1 circularity; intact: ≥ 20 μm^2 and 0<0.3 circularity)[15].

4.7. Luminex Assay

Cytokines levels were analyzed by Luminex Mouse Discovery Assay (R&D Systems, MN, USA) using a self-designed panel of 12 selected cytokines (plate code: LXSAMSM-12), based on color-coded beads, pre-coated with analyte-specific capture antibodies that permits simultaneous analysis of the analytes. Table S1 detailed cytokines and chemokines of the panel, bead region, sensitivity, and the main functions. Analysis and detection were performed in a Dual-laser flow-based detection instrument, Luminex 200 analyzer by Proyecto Luminex, Programa de Virología, Redeca, ICBM, Facultad de Medicina, Universidad de Chile.

4.8. Electrophysiology

Electrophysiological recordings were performed as described before[73]. Briefly, transverse slices (400 µm) from the dorsal hippocampus were cut under cold artificial cerebrospinal fluid (ACSF, in mM: 124 NaCl, 2.6 $NaHCO_3$, 10 D-glucose, 2.69 KCl, 1.25 KH_2PO_4, 2.5 $CaCl_2$, 1.3 $MgSO_4$, and 2.60 $NaHPO_4$) using a Vibratome (BSK microslicer DTK-1500E, Ted Pella, Redding, CA, USA) and incubated in ACSF for 1 hour at room temperature. In all experiments, 10 µM PTX was added to suppress inhibitory GABAA transmission. Slices were transferred to an experimental chamber (2 ml), superfused (3 ml/min, at room temperature) with gassed ACSF (using 95% O_2/5% CO_2) and visualized by trans-illumination with a binocular microscope (Amscope, Irvine, CA, USA). To evoke field excitatory post synaptic potentials (fEPSPs), Schaffer collaterals were stimulated with bipolar concentric electrodes (Tungsten, 125 µm OD diameter, Microprobes) connected to an isolation unit (Isoflex, AMPI, Jerusalem, Israel). The stimulation was performed in the *stratum radiatum* within 100–200 µm from the recording site. Recordings were filtered at 2.0–3.0 kHz, sampled at 4.0 kHz using an A/D converter (National Instrument, Austin, TX, USA), and stored with the WinLTP program. The basal excitatory synaptic transmission was measured using an input/output curve protocol with 10 s of interval between stimuli. Data were collected and analyzed offline with pClamp 10 software (Molecular Devices, San Jose, CA, USA). To generate LTP, we used high-frequency stimulation (HFS) protocol, which consisted of 3 trains at 100 Hz of stimuli with an inter-train interval of 10 s. Data were collected and analyzed offline with pClamp 10 software (Molecular Devices, San Jose, CA, USA).

4.9. Learning and memory test

Morris water maze (MWM) navigation task was performed to evaluated spatial memory and learning in adult vs aged WT, *Mlkl*-KO and GSK'872-treated mice. Animals were trained in a 1.2-m-diameter

circular pool (opaque water, 50 cm deep) filled with 19-21°C water. A submerged 11.5-cm platform (1 cm below the surface of water, invisible to the animal) was used for training, with a maximum trial duration of 60 s; the mice remained on the platform for 10s at the end of each trial. Each animal was trained to locate the platform for 4 consecutive days following external cues (learning curve), 4 times per day. The test was performed on the fifth day by removing the platform, and swimming was monitored to measure the latency time required to reach the platform and the time spent in each quadrant and in the target quadrant (Q4), and the travelled distance within Q4. Both the learning curve and the test were tracked using an automatic tracking system (ANY-maze video tracking software, Stoelting Co, Wood Dale, IL, USA) to obtain the parameters measured. After testing, the mouse was gently removed from the pool and returned to its cage. Mean heatmaps were generated by the Anymaze software to represent the time spent by different cohorts of mice in a particular location of pool.

4.10. Senescence-associated beta-galactosidase (SA-βgal) activity

Histochemical detection of SA-βgal activity were performed as was described before[74]. Briefly, SA-βgal activity was determined by incubation with 1 mg/mL of solution of 5-bromo-4-chloro-3-indolyl β-d-galactopyranoside in 0.04M citric acid/sodium, 0.005M K_3FeCN_6, 0.005M K_4FeCN_6, 0.15 M NaCl, and 0.002M $MgCl_2$ diluted in phosphate-buffered saline (pH 6) for 16h. After the incubation, hippocampal slices were washed with TBS and mounted in superfrost microscope slides (TermoFisher, 6776214) using Fluoromount-G (TermoFisher, 00-4958-02). Images were taken with Nikon Eclipse E200 optic microscope with 4X and 10X objective magnification. ImageJ software was used to process the images. Positive area for SA-βgal activity was measured and representative images are shown.

4.11. Statistical Analysis

Statistical significance was stablished at $p<0.01$ by one-way ANOVA with Tukey's post-test or two-way ANOVA for multiple comparisons. The analysis was performed using GraphPad Prism Software v8.0 and performed with data obtained from ≥ 3 independent experiments for image analyses and $n \geq 8$ animals for behavioral test.

4.12. Label-free proteomics

S-Trap processing of samples

Samples were processed using S-trap mini protocol (Protifi) (for 310 ug and 110 ug samples) and S-trap micro protocol (for low conc samples) as recommended by the manufacturer with little modification. After, application of the samples on the S-trap mini spin column, trapped proteins were washed 5 times with S-TRAP binding buffer. A double digestion with trypsin (1:40) was carried out first overnight at 37°C in TEAB at a final concentration of 50 mM, and then for another 4 hrs (1:40) in 50mM TEAB. Elution of peptides from S-trap mini spin column was achieved by centrifugation at 1000

x g for 1 min by adding 50 mM TEAB, then 0.2% aqueous formic acid and finally 50% acetonitrile/0.2% formic acid. Resulting tryptic peptides were pooled, dried, and quantified using Pierce Quantitative fluorometric Peptide Assay (Thermo Scientific).

LC-MS methods

1.5 µg peptide was analysed per sample. Samples were injected onto a nanoscale C18 reverse-phase chromatography system (UltiMate 3000 RSLC nano, Thermo Scientific) then electrosprayed into an Q Exactive Plus Mass Spectrometer (Thermo Scientific). For liquid chromatography buffers were as follows: buffer A (0.1% formic acid in Milli-Q water (v/v)) and buffer B (80% acetonitrile and 0.1% formic acid in Milli-Q water (v/v). Sample were loaded at 10 µL/min onto a trap column (100 µm × 2 cm, PepMap nanoViper C18 column, 5 µm, 100 Å, Thermo Scientific) equilibrated in 0.1% trifluoroacetic acid (TFA). The trap column was washed for 5 min at the same flow rate with 0.1% TFA then switched in-line with a µPAC C18 nano-LC column (200 cm, inter-pillar distance- 2.5 µm, pore size- 100-200 Å, PharmaFluidics). The peptides were eluted from the column at a constant flow rate of 300 nl/min with a linear gradient from 3.8% buffer B to 12.5% buffer B in 22 mins, then from 12.5% buffer B to 41.3% buffer B in 95 mins, then from 41.3% buffer B to 61.5% in 23 mins and finally to 100% buffer B in 10 mins. The column was then washed with 100% buffer B for 10 min and re-equilibrated in 1% buffer B for 38 mins. Two blanks were run between each sample to reduce carry-over. The column was kept at a constant temperature of 50^{o}C. The data was acquired using a uPAC-compatible easy spray emitter source operated in positive mode with spray voltage at 2.2 kV, and the ion transfer tube temperature at 275^{o}C. The MS was operated in DIA mode. A scan cycle comprised a full MS scan (m/z range from 345-1155), with RF lens at 60%, AGC target 3E6, orbitrap resolution 70,000, maximum injection time at 200 ms and source fragmentation disabled. The MS survey scan was followed by MS/MS DIA scan events using the following parameters: collision energy mode set to linear with a normalized HCD collision energy set to 25, orbitrap resolution 17500, first fixed mass 200 m/z, AGC target 3E6, maximum injection time 55 ms, isolation windows were variable from 5-66 m/z. The inclusion list (DIA windows) and windows widths are shown in **Table S2**. Data for both MS and MS/MS scans were acquired in profile mode. Mass accuracy was checked before the start of samples analysis.

4.13. Analysis of proteomic data

Data filtering and generation of expression ratios

Raw data files from single-shot label-free experiments were converted into Microsoft Excel workbooks and utilised to generate ratios of protein expression within each animal relative to mean expression of n=4 control animals within each comparison (ie. adult: adult (expression ratio=1), aged: adult, *Mlkl*-KO: aged-WT; aged GSK'872: aged vehicle). Proteins identified by fewer than 2 unique peptides were excluded from subsequent analyses (**Figure S8**) in order to ensure maximum identification confidence. Relative expression ratios per study (ie. aged vs. adult, *Mlkl*-KO vs. aged WT, and aged

GSK'872 vs. aged vehicle) were used for subsequent expression profile clustering analyses. UniProt Accession numbers of proteins identified by 2 or more unique peptides with accompanying expression ratios generated as described above were subjected to expression profile clustering in *BioLayout Express*^{3D}. *BioLayout* utilises a user-determined Pearson correlation and the Markov Clustering Algorithm to cluster input data based on user-determined parameter(s) [75,76]. Pearson correlation was set to 0.97 to cluster datasets into distinct subsets based on similarity in expression profile. Discrete clusters exhibiting biologically relevant expression profiles- ie. opposing directionality between aged versus both MLKL-KO and GSK'872 expression ratios (**Fig S8 and Fig S9**) were identified and exported as .txt files containing and identifier column and expression ratios, for subsequent analyses in IPA.

Ingenuity Pathway Analysis (IPA)

The Ingenuity Pathway Analysis (IPA) application (Ingenuity Systems, Silicon Valley, CA) was used to visualise and explore the cellular and molecular pathways that may have been altered as result of genetic (*Mlkl*-KO) or pharmacological (GSK'872) inhibition of necroptosis. Without user-directed manipulation, IPA's statistical predictions and annotations are approximately 90% based off on peer-reviewed publications; the remaining 10% of stored interactions have been identified by other in silico techniques. The analyses were performed only using experimentally reported interactions published in peer-reviewed publications stored within the "hand-curated" and continually updated Ingenuity Knowledge database (Ingenuity Systems, Silicon Valley, CA). For more information on the computational methodology underpinning IPA, please refer to http://www.ingenuity.com/.

Prior to all analyses within IPA, input datasets comprising, as described above, mean expression ratios of n=4 animals per experimental group, were converted to fold-change values, and a ±20% cut-off in expression change respective to control was applied within each respective study. Individual analyses of aged vs. adult, *Mlkl*-KO vs. WT, and GSK'872 vs. vehicle were performed prior to a comparative analysis in order to gain insight into potential biological networks distinguishing "normal" versus "necroptosis-inhibited" aging processes.

For canonical pathway analysis, p-values of canonical pathway scores and subsequent ranking for all analyses performed in this study were derived from a Fisher's Exact Test calculating overlap between molecules in each respective input dataset and number of molecules comprising canonical pathway as defined by the Ingenuity Systems Database. Predicted activation z-scores were calculated by weighing the predicted expression change of target molecules as defined by Ingenuity Knowledge Database against the actual expression change of target molecules reported in input dataset. An activation z-score >2 or <−2 is considered statistically significant (Ingenuity Systems, Silicon Valley, CA). Constituent molecules within pathway were colourized with intensity of colour corresponding to magnitude of change.

For diseases and functions analysis, predicted activation z-scores of associated downstream diseases and functions were calculated by weighing the predicted expression change of target

molecules associated with specific "diseases or functions" annotation as defined by Ingenuity Knowledge Database against the actual expression change of target molecules reported in input datasets. An activation z-score >2 or <−2 is considered statistically significant. *P*-values of overlap is derived from a Fisher's exact test were derived from a Fisher's Exact Test calculating overlap between molecules in each respective input dataset and number of molecules comprising the known interactome of each regulator as defined by Ingenuity Systems Database. In graphical format, target molecules present within each proteomic dataset predicted to be activated or inhibited to mediate the associated "diseases or functions" annotation were visualised in relation to their associated predicted regulator and were colourised with intensity of colour corresponding to magnitude of change.

Funding and acknowledgement

This work was supported by grants from the Geroscience Center for Brain Health and Metabolism, FONDAP- 15150012 (to FAC and CC), Fondo Nacional de Desarrollo Científico y Tecnológico (FONDECYT) N° 1150766 (to FAC), Michael J Fox Foundation for Parkinson's Research 17303 (to FAC), Agencia Nacional de Investigación y Desarrollo (ANID) FONDECYT Postdoctorado N° 3180313 (to MSA), BBSRC ISP funding (BBS/E/D/10002071) (to TMW and SLE), BBSRC EastBio (to SI), EMC (to RAK), Centro Científico y Tecnológico Ciencia & Vida, FB210008, Financiamiento Basal para Centros Científicos y Tecnológicos de Excelencia de ANID (to SB), Fondo Nacional de Desarrollo Científico y Tecnológico (FONDECYT) N° 1190620 (to WC), Center for Excellence in Science and Technology AFB 170005, PFB 12/2007 (to WC), Fondo Nacional de Desarrollo Científico y Tecnológico (FONDECYT) N° 1200255 to CC, and a PhD fellowship by ANID (to ML).

Data availability statement

Raw data from Fig 1,2,3,4,5,6 and 8 are available as an extended excel file named "Figures Raw Data".Raw data from Supplementary Figures S1, S2, S3, S4, S5, S6 and S11 are available as an extended excel file named "Suppl Figures Raw Data". The datasets generated from the proteomic analysis are available in the data repository of Edinburgh University with an assigned DOI. All the data that support the findings of this study are also available from the corresponding author upon request.

References

1. Aburto, J. M., Villavicencio, F., Basellini, U., Kjærgaard, S. & Vaupel, J. W. Dynamics of life expectancy and life span equality. *Proc. Natl. Acad. Sci. U. S. A.* **117**, 5250–5259 (2020).

2. Hansen, M. & Kennedy, B. K. Does Longer Lifespan Mean Longer Healthspan? *Trends in Cell Biology* vol. 26 565–568 (2016).

3. Duan, J. *et al.* Association of cognitive impairment and elderly mortality: Differences between two cohorts ascertained 6-years apart in China. *BMC Geriatr.* **20**, 29 (2020).

4. Agüero-Torres, H., Thomas, V. S., Winblad, B. & Fratiglioni, L. The impact of somatic and cognitive disorders on the functional status of the elderly. *J. Clin. Epidemiol.* **55**, 1007–1012 (2002).

5. Wyss-Coray, T. Ageing, neurodegeneration and brain rejuvenation. *Nature* **539**, 180–186 (2016).

6. O'Shea, A., Cohen, R. A., Porges, E. C., Nissim, N. R. & Woods, A. J. Cognitive aging and the hippocampus in older adults. *Front. Aging Neurosci.* **8**, (2016).

7. Wimmer, M. E., Hernandez, P. J., Blackwell, J. & Abel, T. Aging impairs hippocampus-dependent long-term memory for object location in mice. *Neurobiol. Aging* **33**, 2220–2224 (2012).

8. Geinisman, Y., de Toledo-Morrell, L., Morrell, F., Persina, I. S. & Rossi, M. Age-related loss of axospinous synapses formed by two afferent systems in the rat dentate gyrus as revealed by the unbiased stereological dissector technique. *Hippocampus* **2**, 437–444 (1992).

9. Barnes, C. A. & McNaughton, B. L. Physiological compensation for loss of afferent synapses in rat hippocampal granule cells during senescence. *J. Physiol.* **309**, 473–485 (1980).

10. Rosenzweig, E. S. & Barnes, C. A. *Impact of aging on hippocampal function: Plasticity, network dynamics, and cognition*. *Progress in Neurobiology* vol. 69 (2003).

11. Peters, A., Moss, M. B. & Sethares, C. Effects of aging on myelinated nerve fibers in monkey primary visual cortex. *J. Comp. Neurol.* **419**, 364–76 (2000).

12. Stahon, K. E. *et al.* Age-Related Changes in Axonal and Mitochondrial Ultrastructure and Function in White Matter. *J. Neurosci.* **36**, 9990–10001 (2016).

13. Radhakrishnan, H., Stark, S. M. & Stark, C. E. L. Microstructural Alterations in Hippocampal Subfields Mediate Age-Related Memory Decline in Humans. *Front. Aging Neurosci.* **12**, 1–15 (2020).

14. Marner, L., Nyengaard, J. R., Tang, Y. & Pakkenberg, B. Marked loss of myelinated nerve fibers in the human brain with age. *J. Comp. Neurol.* **462**, 144–152 (2003).

15. Arrázola, M. S. *et al.* Axonal Degeneration Is Mediated by Necroptosis Activation. *J. Neurosci.* **39**, 3832–3844 (2019).

16. Hernández, D. E. *et al.* Axonal degeneration induced by glutamate excitotoxicity is mediated by necroptosis. *J. Cell Sci.* **131**, jcs214684 (2018).

17. Gerdts, J., Summers, D. W., Sasaki, Y., DiAntonio, A. & Milbrandt, J. Sarm1-Mediated Axon Degeneration Requires Both SAM and TIR Interactions. *J. Neurosci.* **33**, 13569–13580 (2013).

18. Osterloh, J. M. *et al.* dSarm/Sarm1 is required for activation of an injury-induced axon death pathway. *Science* **337**, 481–4 (2012).

19. Ko, K. W., Milbrandt, J. & DiAntonio, A. SARM1 acts downstream of neuroinflammatory and necroptotic signaling to induce axon degeneration. *J. Cell Biol.* **219**, (2020).

20. Holler, N. *et al.* Fas triggers an alternative, caspase-8-independent cell death pathway using the kinase RIP as effector molecule. *Nat. Immunol.* **1**, 489–95 (2000).

21. Seo, J., Nam, Y. W., Kim, S., Oh, D.-B. & Song, J. Necroptosis molecular mechanisms: Recent findings regarding novel necroptosis regulators. *Exp. Mol. Med. 2021 536* **53**, 1007–1017 (2021).

22. Samson, A. L. *et al.* MLKL trafficking and accumulation at the plasma membrane control the kinetics and threshold for necroptosis. *Nat. Commun.* **11**, 3151 (2020).

23. Kennedy, B. K. *et al.* Geroscience: Linking aging to chronic disease. *Cell* **159**, 709–713 (2014).

24. Franceschi, C. & Campisi, J. Chronic inflammation (Inflammaging) and its potential contribution to age-associated diseases. *Journals Gerontol. - Ser. A Biol. Sci. Med. Sci.* **69**, S4–S9 (2014).

25. López-Otín, C., Blasco, M. A., Partridge, L., Serrano, M. & Kroemer, G. The hallmarks of aging. *Cell* vol. 153 1194 (2013).

26. Li, D. *et al.* RIPK1-RIPK3-MLKL-dependent necrosis promotes the aging of mouse male reproductive system. *Elife* **6**, 1–21 (2017).

27. Deepa, S. S., Unnikrishnan, A., Matyi, S., Hadad, N. & Richardson, A. Necroptosis increases with age and is reduced by dietary restriction. *Aging Cell* **17**, 1–5 (2018).

28. Re, D. B. *et al.* Necroptosis Drives Motor Neuron Death in Models of Both Sporadic and Familial ALS. *Neuron* **81**, 1001–1008 (2014).

29. Ito, Y. *et al.* RIPK1 mediates axonal degeneration by promoting inflammation and necroptosis in ALS. *Science* **353**, 603–8 (2016).

30. Iannielli, A. *et al.* Pharmacological Inhibition of Necroptosis Protects from Dopaminergic Neuronal Cell Death in Parkinson's Disease Models. *Cell Rep.* **22**, 2066–2079 (2018).

31. Oñate, M. *et al.* The necroptosis machinery mediates axonal degeneration in a model of Parkinson disease. *Cell Death Differ.* **27**, 1169–1185 (2020).

32. Caccamo, A. *et al.* Necroptosis activation in Alzheimer's disease. *Nat. Neurosci.* **20**, 1236–1246 (2017).

33. Thadathil, N. *et al.* Necroptosis increases with age in the brain and contributes to age-related neuroinflammation. *GeroScience* **43**, 2345–2361 (2021).

34. Kassab, R. & Alexandre, F. Pattern separation in the hippocampus: distinct circuits under different conditions. *Brain Struct. Funct.* **223**, 2785–2808 (2018).

35. Nadeem, M. *et al.* Immunolabelling of non-phosphorylated neurofilament indicates damage of spinal cord axons in TSE-infected goats. *Vet. Rec.* **178**, 141.1-141 (2016).

36. Petzold, A. Neurofilament phosphoforms: Surrogate markers for axonal injury, degeneration and loss. *J. Neurol. Sci.* **233**, 183–198 (2005).

37. Finn, J. T. *et al.* Evidence that Wallerian degeneration and localized axon degeneration induced by local neurotrophin deprivation do not involve caspases. *J. Neurosci.* **20**, 1333–41 (2000).

38. Whitmore, A. V, Lindsten, T., Raff, M. C. & Thompson, C. B. The proapoptotic proteins Bax and Bak are not involved in Wallerian degeneration. *Cell Death Differ.* **10**, 260–261 (2003).

39. Yoon, S., Bogdanov, K., Kovalenko, A. & Wallach, D. Necroptosis is preceded by nuclear translocation of the signaling proteins that induce it. *Cell Death Differ.* **23**, 253–260 (2016).

40. Spiegel, A. M., Koh, M. T., Vogt, N. M., Rapp, P. R. & Gallagher, M. Hilar interneuron vulnerability distinguishes aged rats with memory impairment. *J. Comp. Neurol.* **521**, 3508–3523 (2013).

41. Wu, J. *et al.* Mlkl knockout mice demonstrate the indispensable role of Mlkl in necroptosis. *Nat. Publ. Gr.* **23**, 994–1006 (2013).

42. Hwang, I. *et al.* FOXO protects against age-progressive axonal degeneration. *Aging Cell* **17**, 1–100 (2018).

43. Yang, W., Zhou, X. & Ma, T. Memory Decline and Behavioral Inflexibility in Aged Mice Are Correlated With Dysregulation of Protein Synthesis Capacity. *Front. Aging Neurosci.* **11**, 246 (2019).

44. Burke, S. N. & Barnes, C. A. Neural plasticity in the ageing brain. *Nat Rev Neurosci* **7**, 30–40 (2006).

45. Salvadores, N. & Court, F. A. The necroptosis pathway and its role in age-related neurodegenerative diseases: will it open up new therapeutic avenues in the next decade? *Expert Opin. Ther. Targets* **24**, 679–693 (2020).

46. Yang, X. S. *et al.* Hypoxia-inducible factor-1 alpha is involved in RIP-induced necroptosis caused by in vitro and in vivo ischemic brain injury. *Sci. Rep.* **7**, 1–11 (2017).

47. Orozco, S. & Oberst, A. RIPK3 in cell death and inflammation: the good, the bad, and the ugly.

Immunol. Rev. **277**, 102–112 (2017).

48. Bouchard, J. & Villeda, S. A. Aging and brain rejuvenation as systemic events. *J. Neurochem.* **132**, 5–19 (2015).

49. Lynch, G., Rex, C. S. & Gall, C. M. Synaptic plasticity in early aging. *Ageing Res. Rev.* **5**, 255–280 (2006).

50. Wang, C. *et al.* DNA damage response and cellular senescence in tissues of aging mice. *Aging Cell* **8**, 311–323 (2009).

51. Jurk, D. *et al.* Postmitotic neurons develop a p21-dependent senescence-like phenotype driven by a DNA damage response. *Aging Cell* **11**, 996 (2012).

52. Gorostieta-Salas, E. *et al.* Enhanced Activity of Exportin-1/CRM1 in Neurons Contributes to Autophagy Dysfunction and Senescent Features in Old Mouse Brain. *Oxid. Med. Cell. Longev.* **2021**, 1–22 (2021).

53. Pruitt, S. C., Freeland, A., Rusiniak, M. E., Kunnev, D. & Cady, G. K. Cdkn1b overexpression in adult mice alters the balance between genome and tissue ageing. *Nat. Commun.* **4**, 2626 (2013).

54. Ropireddy, D., Scorcioni, R., Lasher, B., Buzsáki, G. & Ascoli, G. A. Axonal morphometry of hippocampal pyramidal neurons semi-automatically reconstructed after in vivo labeling in different CA3 locations. *Brain Struct. Funct.* **216**, 1–15 (2011).

55. West, M. J. Regionally specific loss of neurons in the aging human hippocampus. *Neurobiol. Aging* **14**, 287–293 (1993).

56. Santhakumar, V. *et al.* Granule cell hyperexcitability in the early post-traumatic rat dentate gyrus: The 'irritable mossy cell' hypothesis. *J. Physiol.* **524**, 117–134 (2000).

57. Scharfman, H. E. The enigmatic mossy cell of the dentate gyrus. *Nat. Rev. Neurosci.* **17**, 562–575 (2016).

58. Amani, M. *et al.* Rapid Aging in the Perforant Path Projections to the Rodent Dentate Gyrus. *J. Neurosci.* **41**, JN-RM-2376-20 (2021).

59. Dillon, S. E. *et al.* The impact of ageing reveals distinct roles for human dentate gyrus and CA3 in pattern separation and object recognition memory. *Sci. Rep.* **7**, 1–13 (2017).

60. Choi, M. E., Price, D. R., Ryter, S. W. & Choi, A. M. K. Necroptosis: A crucial pathogenic mediator of human disease. *JCI Insight* vol. 4 (2019).

61. Hagan, C. When are mice considered old? https://www.jax.org/news-and-insights/jax-blog/2017/november/when-are-mice-considered-old# (2017).

804 62. Rocca, W. A. *et al.* Trends in the incidence and prevalence of Alzheimer's disease, dementia,
805 and cognitive impairment in the United States. *Alzheimer's Dement.* **7**, 80–93 (2011).

806 63. Barrientos, R. M., Kitt, M. M., Watkins, L. R. & Maier, S. F. Neuroinflammation in the normal
807 aging hippocampus. *Neuroscience* **309**, 84–99 (2015).

808 64. Hofer, M., Hausmann, J., Staeheli, P. & Pagenstecher, A. Cerebral expression of interleukin-12
809 induces neurological disease via differential pathways and recruits antigen-specific T cells in
810 virus-infected mice. *Am. J. Pathol.* **165**, 949–958 (2004).

811 65. Chen, Z. *et al.* IL-12p35 deficiency alleviates kainic acid-induced hippocampal
812 neurodegeneration in C57BL/6 mice. *Neurobiol. Dis.* **17**, 171–178 (2004).

813 66. Lobo-Silva, D., Carriche, G. M., Castro, A. G., Roque, S. & Saraiva, M. Balancing the immune
814 response in the brain: IL-10 and its regulation. *Journal of Neuroinflammation* vol. 13 1–10 (2016).

815 67. Bettio, L. E. B., Rajendran, L. & Gil-Mohapel, J. The effects of aging in the hippocampus and
816 cognitive decline. *Neuroscience and Biobehavioral Reviews* vol. 79 66–86 (2017).

817 68. Hodgson, R. *et al.* Aging: therapeutics for a healthy future. *Neuroscience and Biobehavioral*
818 *Reviews* vol. 108 453–458 (2020).

819 69. Partridge, L., Fuentealba, M. & Kennedy, B. K. The quest to slow ageing through drug discovery.
820 *Nature Reviews Drug Discovery* vol. 19 513–532 (2020).

821 70. Zia, A., Pourbagher-Shahri, A. M., Farkhondeh, T. & Samarghandian, S. Molecular and cellular
822 pathways contributing to brain aging. *Behav. Brain Funct. 2021 171* **17**, 1–30 (2021).

823 71. Murphy, J. M. *et al.* The pseudokinase MLKL mediates necroptosis via a molecular switch
824 mechanism. *Immunity* **39**, 443–453 (2013).

825 72. Flurkey, K., Currer, J. M. & Harrison, D. E. Mouse Models in Aging Research. in *The Mouse in*
826 *Biomedical Research* vol. 3 637–672 (Elsevier Inc., 2007).

827 73. Carvajal, F. J., Mira, R. G., Rovegno, M., Minniti, A. N. & Cerpa, W. Age-related NMDA signaling
828 alterations in SOD2 deficient mice. *Biochim. Biophys. Acta - Mol. Basis Dis.* **1864**, 2010–2020
829 (2018).

830 74. Debacq-Chainiaux, F., Erusalimsky, J. D., Campisi, J. & Toussaint, O. Protocols to detect
831 senescence-associated beta-galactosidase (SA-βgal) activity, a biomarker of senescent cells in
832 culture and in vivo. *Nat. Protoc.* **4**, 1798–1806 (2009).

833 75. Enright, A. J. An efficient algorithm for large-scale detection of protein families. *Nucleic Acids*
834 *Res.* **30**, 1575–1584 (2002).

835 76. Theocharidis, A., van Dongen, S., Enright, A. J. & Freeman, T. C. Network visualization and
836 analysis of gene expression data using BioLayout Express3D. *Nat. Protoc.* **4**, 1535–1550 (2009).

837

Figure 1

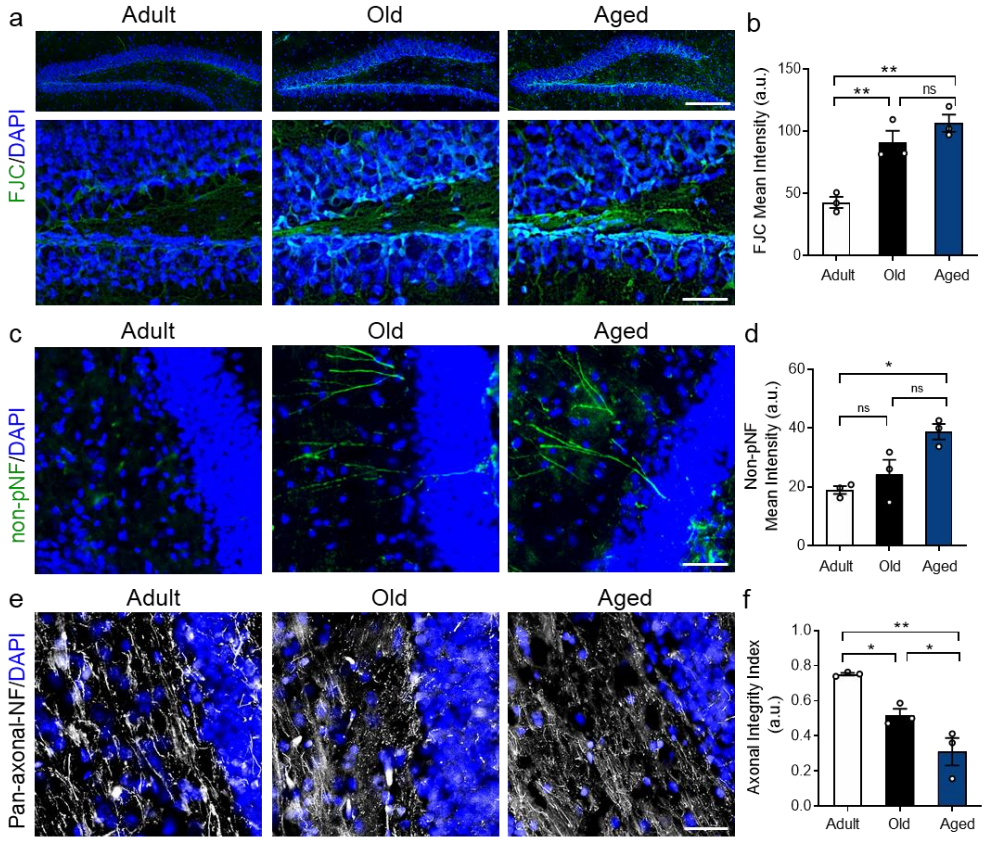

Fig 1. Increased axonal degeneration in the hippocampus during aging. Representative images of hippocampal sections from adult (3-6 month), old (12-25 month) and aged mice (more than 24 month) stained with Fluoro Jade C (FJC, green), non-phosphorylated neurofilament (non-pNF) and pan-axonal NF **(a,c,e)**. Nuclear staining with DAPI (blue) was used to identify the granular layer. **(b,d)** The mean fluorescence intensity was evaluated in FJC and non-pNF staining to determine levels of neurodegeneration in the hilus according to age. **(f)** Axonal degeneration was assessed in the DG hilus using the axonal integrity index in hippocampal sections immunostained with the pan-axonal NF antibody. Calibration bars, 250 µm (entire DG) and 50 µm for magnified hippocampal images. Values are the result of the analysis of n=3-4 mice per group. One-way ANOVA with Tukey analysis for multiple comparisons, *p:<0.05; **p<0.01; ***p<0.005; ****p<0.001.

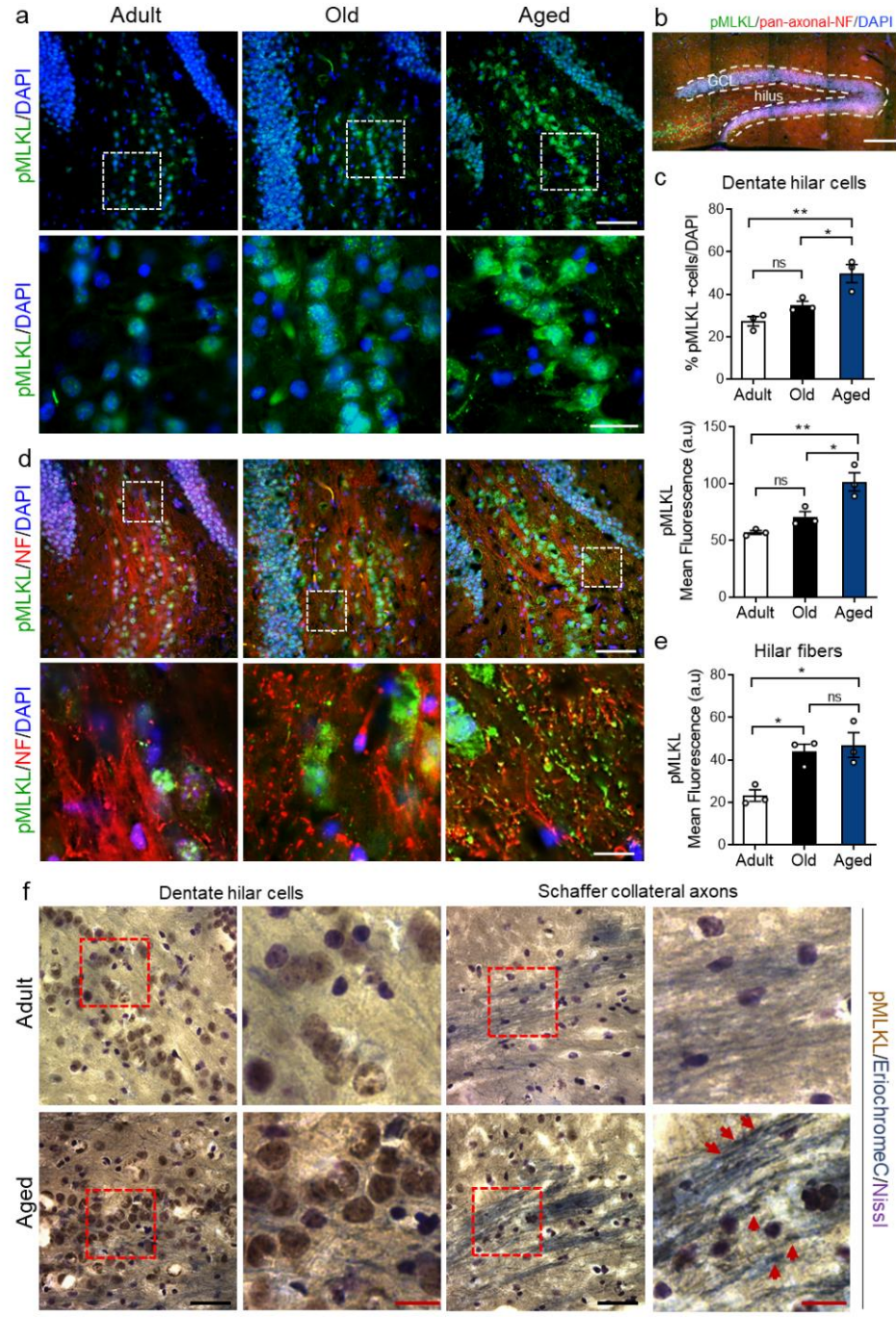

Fig 2. Progressive increase of phosphorylated MLKL levels in the hippocampal hilus along aging. (a) MLKL phosphorylation at serine 345 (green) was evaluated in adult (3-6 month), old (12-25 month) and aged mice (more than 24 month) (bar=25 µm and 10 µm for magnification). **(b)** Mosaic reconstruction of the hippocampal dentate gyrus (DG) illustrates each subfield: the granular cell layer (GCL), and the hilus, showing pMLKL in green (bar=100 µm). **(c)** Quantification of pMLKL signal in hilar cells is plotted as the percentage of pMLKL positive cells normalized against the total cell number in the hilar area (upper graph), and as pMLKL mean intensity (lower graph). **(d)** Axonal pMLKL was detected in NF-positive axons in the hilus, dotted boxes illustrate magnified areas shown in the bottom panel. Calibration bars, 25 µm and 5 µm for inset. **(e)** pMLKL mean intensity was analyzed in hilar fibers along aging. Error bars, mean ± SEM, *p:<0.05; **p<0.01. Statistical significance was determined by one-way ANOVA with Tukey analysis for multiple comparisons. **(f)** Immunohistochemistry against pMLKL (brown) and Eriochrome-C staining (myelinated axons, blue). Calibration bar 40 µm. Red dotted boxes showed image magnification of each condition. Calibration bar, 15 µm. Necroptosis activation in DG axons and in Schaffer collateral projections of the hippocampus are shown with red arrowheads. Increased pMLKL was also observed in neuronal somas (dark brown/+Nissl, violet).

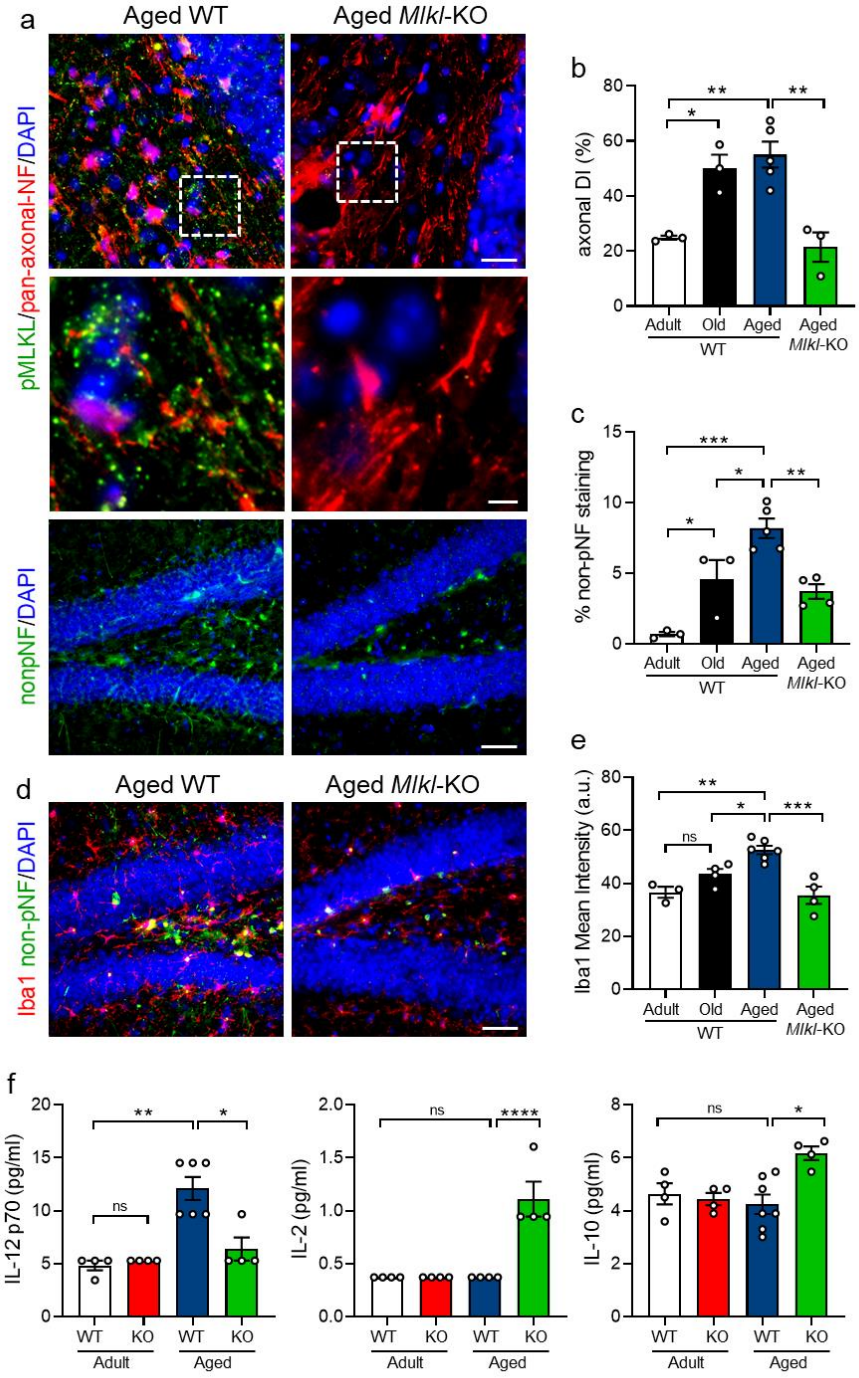

Fig 3. *Mlkl* deficiency protects the brain from age-associated axonal degeneration and neuroinflammation. Axonal degeneration and neuroinflammation were evaluated in the DG hilus of aged WT and *Mlkl*-KO mice and compared with the values of the normal aging curve (N= 3-5 mice per group). **(a)** Axonal degeneration was detected by immunostaining of axons with the pan-axonal-NF marker (red) and evaluated by calculating the axonal degeneration index (DI). Calibration bars, 25 µm and 5µm for insets. **(b)** Increased non-pNF signal was also used as a positive marker of axonal degeneration. Calibration, bar, 50 µm. **(c)** Quantification of non-pNF signal plotted as the percentage of stained area in the hilus. **(d)** Microglia activation was measured by Iba1 immunodetection. Calibration bar, 50 µm. **(e)** Microglia activation quantified through Iba1 mean intensity. **(f)** Cytokines levels in the hippocampus of adult versus aged WT and *Mlkl*-KO mice were assessed by Luminex High Performance Assay. Plots represent absolute cytokine levels (pg/ml), including IL-12, IL-2 and IL-10 in aged WT and *Mlkl*-KO hippocampus, (N=4-7 mice per group). Error bars, mean ± SEM, *p:<0.05; **p<0.01; ***p<0.005; ****p<0.001. Statistical significance was determined by one-way ANOVA with Tukey analysis for multiple comparisons.

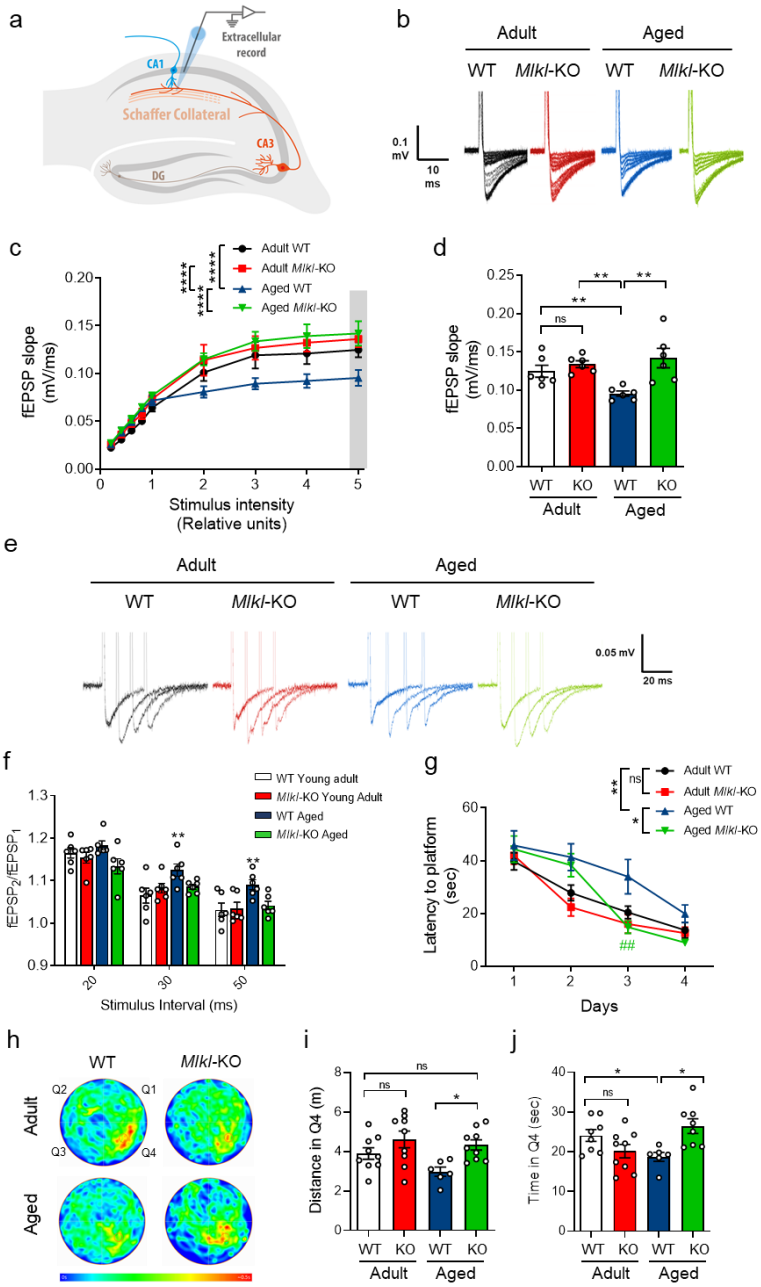

Fig 4. Hippocampal function and memory are improved in aged *Mlkl*-KO mice. (a) Field excitatory post synaptic potential (fEPSP) was measured in hippocampal slices in the CA3-CA1 circuit as described in the scheme. **(b,c)** Average traces of the evoked potentials recorded in each condition were used to plot the fEPSP slope upon several stimulus intensity. **(d)** The average fEPSP slope at the highest stimulus (gray bar in c) was plotted as bar graphs, showing significant differences between groups. **(e,f)** Paired pulse facilitation was measured as the facilitation index ($fEPSP_2/fEPSP_1$). Values are the result of the analysis of N=3 mice per group (n=3 slices per mice). Error bars, mean ± SEM, **p<0.01. Statistical significance was determined by one-way ANOVA. Hippocampal-dependent behavioral function was evaluated using the standard Morris water maze (MWM) navigation task. **(g)** Escape latency was measured as the time to reach the hidden platform during the learning curve in aged and adult WT vs *Mlkl*-KO mice. **(h)** Mean heatmaps specify location each mice cohort along time in pseudo-color during memory testing (day 5). The quadrant Q4 designates the initial location of the hidden platform during training. **(i,j)** Travelled distance and time spent in Q4, respectively. Values are the result of the analysis of n=7-10 mice per group. One-way ANOVA with Tukey correction for multiple comparison, *p:<0.01; Two-way ANOVA plus Sidak's multiple comparison test was applied for the learning curve data analysis. Significance between curves was determined with a *p=0.0209 for aged WT and *Mlkl*-KO comparison, and **p=0.0015 for differences between adult and aged WT mice. Differences observed at day 3 between aged WT vs *Mlkl*-KO correspond to ##p=0.0043.

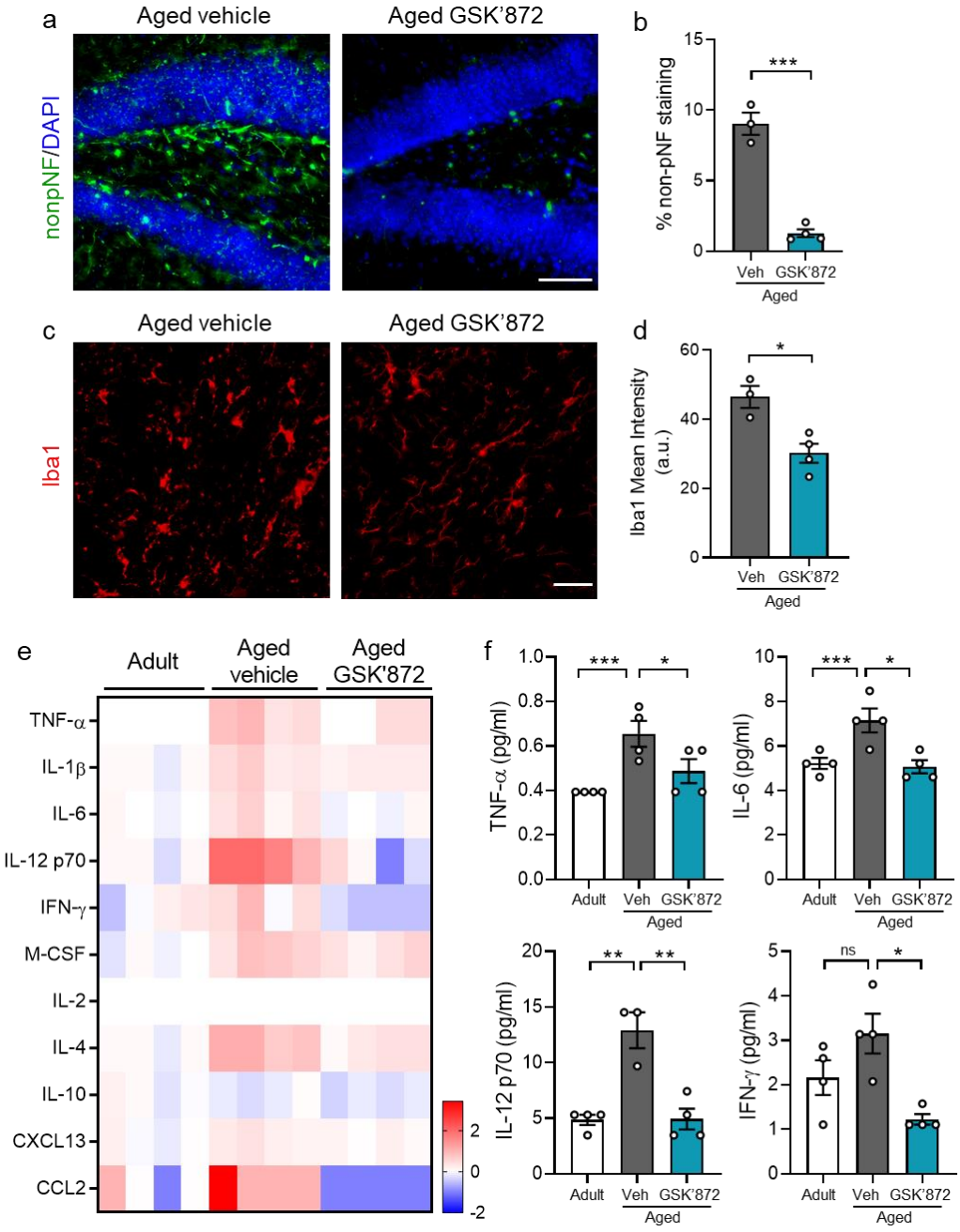

Fig 5. Short-term and systemic RIPK3 inhibition reverts age-associated axonal degeneration and neuroinflammation. Aged mice (23-month-old) treated with vehicle or GSK'872, intraperitoneally delivered through an osmotic pump, diffusion rate = 0.11 µl/hr/28 days. **(a,b)** Axonal degeneration detected by non-pNF (calibration bar, 50 µm) was quantified and plotted as the percentage of stained area in the DG hilus. **(c,d)** Microglia activation assessed by Iba1 immunodetection (calibration bar, 50µm) and quantified as Iba1 mean intensity in the hilus. **(e)** The heatmap shows fold change levels of cytokines and chemokines analyzed in the hippocampus of adult versus aged-vehicle and aged-GSK'872 treated mice (n =4, separated in each column). **(f)** Absolute levels (pg/ml) of TNF-α, IL-6, IL-12p70 and IFN-γ in the hippocampus of adult (white bar), aged-vehicle (gray) and aged-GSK'872 (light blue) treated mice. (N=3-4 mice per group). Error bars, mean ± SEM, *p:<0.05; **p<0.01; ***p<0.005. Statistical significance was determined by one-way ANOVA with Tukey analysis for multiple comparisons.

Figure 6

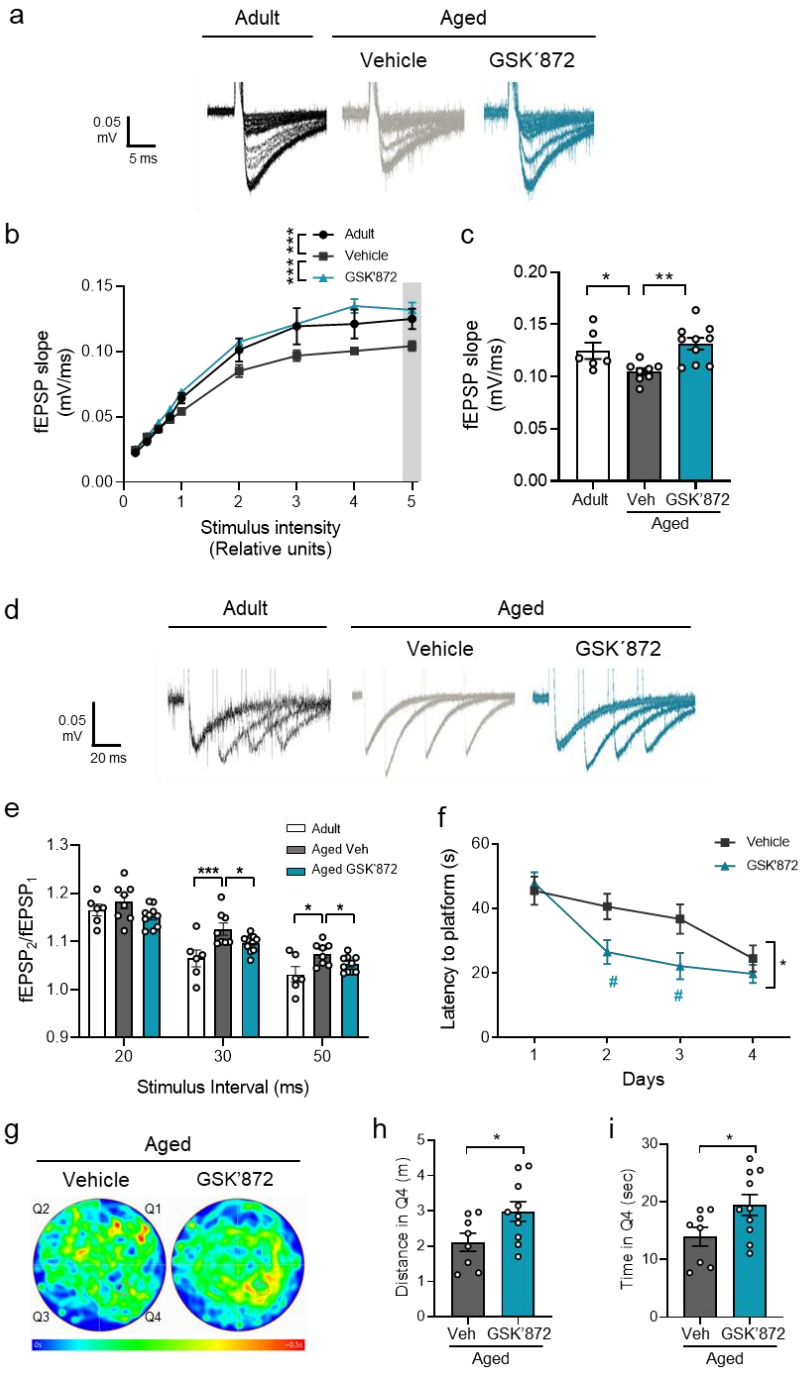

Fig 6. Pharmacological necroptosis inhibition restores hippocampal function and memory in aged mice. (a) Average traces of the evoked potentials recorded in each condition were used to plot the fEPSP slope upon several stimulus intensity in b. **(c)** The average fEPSP slope at the highest stimulus (gray bar in **a**) was plotted. Significant differences were detected between groups. **(d,e)** Paired pulse facilitation was measured as the facilitation index ($fEPSP_2/fEPSP_1$). Values are the result of the analysis of N=3 mice per group (n=3 slices per mice). Error bars, mean ± SEM, **p<0.01. Statistical significance was determined by one-way ANOVA. Hippocampal-dependent memory was evaluated with the MWM test. **(f)** Escape latency of vehicle-treated vs GSK'872-treated aged mice measured during the learning curve. **(g)** The swimming heatmaps indicating the average mice location along time (pseudo-color) during memory testing (day 5) show increased preference of aged mice treated with GSK'872 to the original location of the platform (Q4) compared with aged-vehicle mice. **(h, i)** Travelled distance and the time spent in the target quadrant Q4 were plotted. Values are the result of the analysis of n=8-10 mice. T-test with Welch's correction, *p:<0.01. Two-way ANOVA with Sidak's multiple comparison test was applied for the learning curve data. Significance between both curves was determined with a *p=0.0259. Differences between vehicle vs GSK'872 at day 2 and 3 correspond to $^{\#}$p=0.0210 and p=0.0328, respectively.

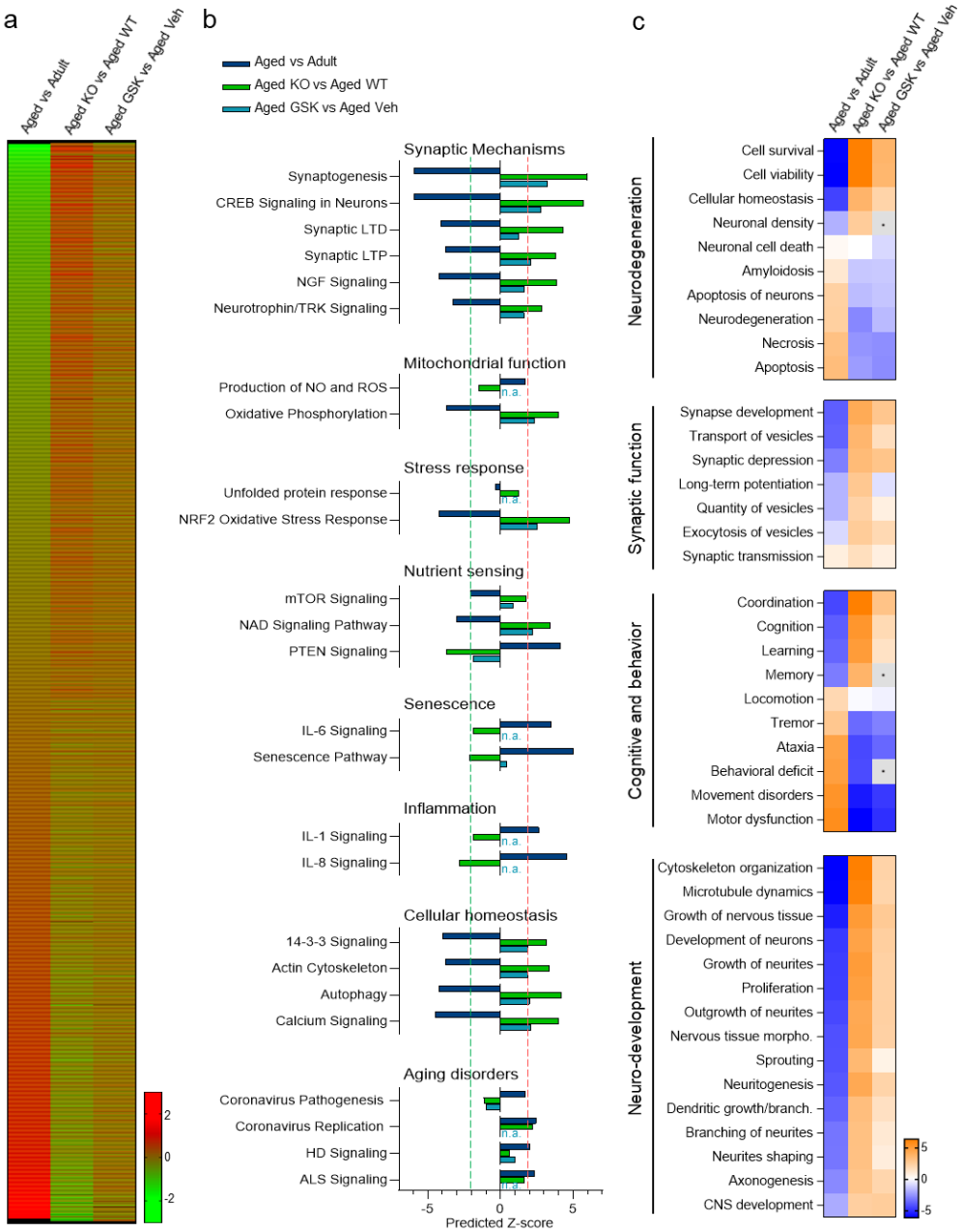

Fig 7. Proteomic analysis reveals opposing directionality in protein expression and aging-associated biofunctions between normal aging and necroptosis-targeted inhibition. (a) Heat map illustrating proteins exhibiting opposing directionality in expression between "normal" aging (aged vs. adult) and necroptosis-inhibited processes in aged mice (*Mlkl*-KO and GSK'872), as identified through unbiased expression profile clustering **(Fig S8 and Fig S9)**. Heat map depicts mean expression ratio (log 2) of *n*=4 mice per experimental group versus their respective controls. Red represents upregulation compared to control within each respective analysis, while green represents downregulation. **(b)** Selection of canonical pathways classified as aging hallmarks **(Supplementary Fig S10)** were identified through comparative analyses of proteins correlating with necroptosis-targeted inhibition of aging phenotypes. Opposing directionality was observed in predicted activation or inhibition scores between "normal" aging cohort, and both *Mlkl*-KO or GSK'872-treated mice. A predicted z-score >2 or <-2 (indicated by dotted lines) is considered statistically significant. For description of statistical tests utilized to generate predictive z-score see Methods. **(c)** Selected diseases and biofunctions implicated in brain rejuvenation and derived through comparative analyses of proteins correlating with necroptosis-targeted inhibition of aging phenotypes. Heatmaps shows the opposing directionality in predicted activation or inhibition scores between "normal" aging, and both *Mlkl*-KO or GSK'872-treated mice. For description of statistical tests utilized to generate predictive z-scores, see Methods.

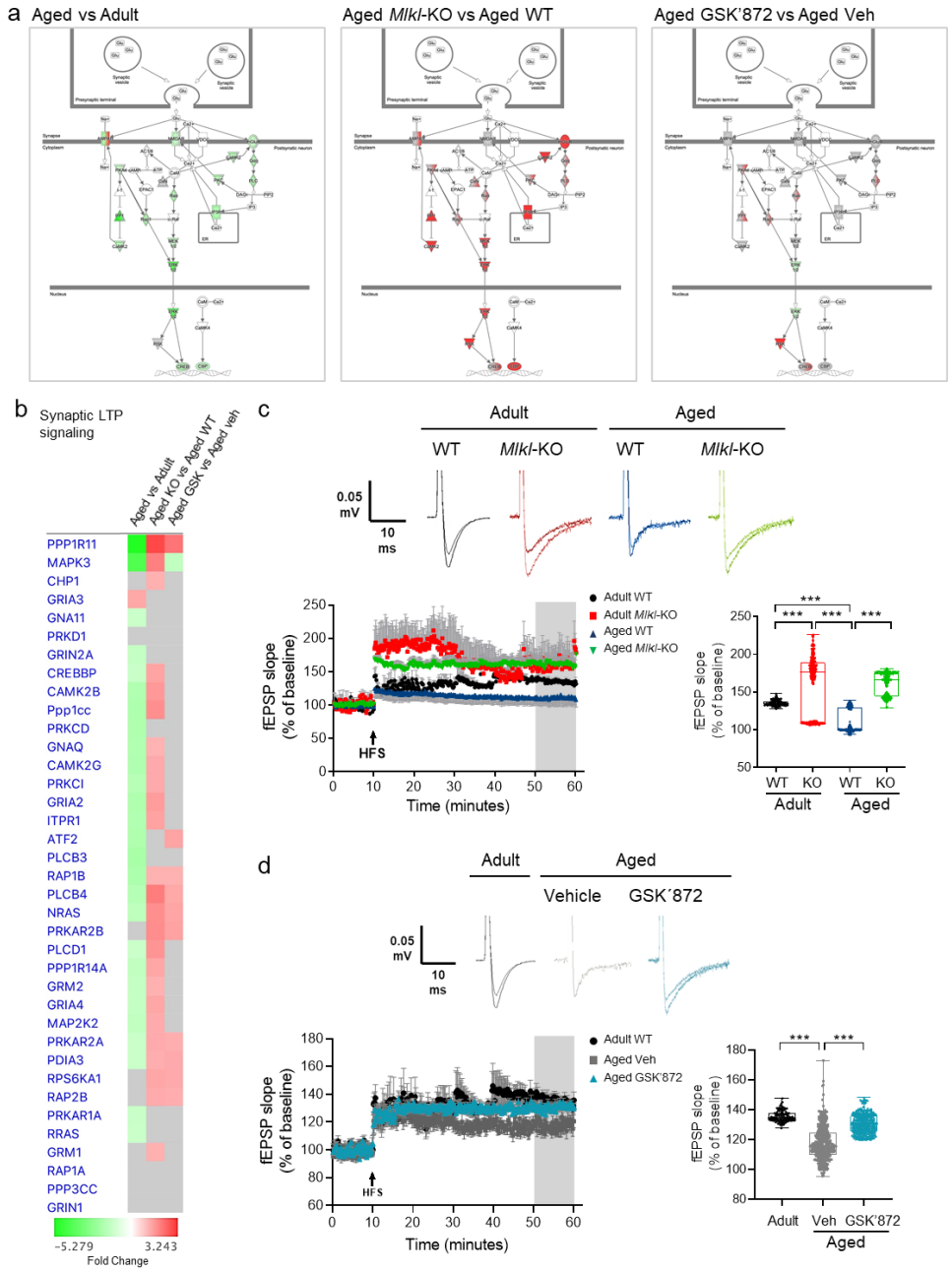

Fig 8. Increased synaptic long-term potentiation in the necroptosis-inhibited aging process. Schematic illustrating the canonical pathway annotation of "Synaptic long-term potentiation signaling". Top canonical pathway annotations were defined by ranking of absolute z-score between "normal" aging, *Mlkl*-KO and GSK'872 analyses. Intensity of colour represents magnitude of change; red corresponds to upregulation compared to control within each respective analysis, while green represents downregulation. Molecules in grey were identified to be necroptosis-correlative alterations present within input dataset, but fell below the 20% cut-off, while molecules in white were not present within input dataset (See Supplementary Figures S8, S9) but changed less than 20% in analysis. Solid connecting lines represent a direct interaction, while dashed connecting lines indicate an indirect interaction. **(b)** Heat map of individual proteins assigned to the canonical pathway "Synaptic long-term potentiation signaling". Changes between normal aging and *Mlkl*-KO or GSK'872 treated mice were expressed as fold change. **(c)** Canonical pathway annotation "Synaptic long-term potentiation signaling". Synaptic plasticity was evaluated by LTP magnitude measurement, generated by high-frequency stimulation (HFS) in the hippocampal CA1 area of WT and *Mlkl*-KO mice from adult and aged groups. fEPSP slope was plotted as individual values considering the last 10 minutes of the recording. **(d)** "Synaptic LTP signaling" in aged mice treated with GSK'872 vs vehicle. LTP was generated by HFS in the CA1-CA3 hippocampal transmission and registered for 1h. The last 10 minutes of fEPSP slope were plotted as boxes to evaluate statistical differences. Values are the result of the analysis of N=4 mice per group (n=8-10 slices per mice). Error bars, mean ± SEM, ***p<0.005. Statistical significance was determined by one-way ANOVA.